

# Chronic cerebral hypoperfusion induces venous dysfunction via EPAS1 regulation in mice

Received: 14 May 2024

Accepted: 26 June 2025

Published online: 08 July 2025



Vanessa Kristina Wazny<sup>1,8</sup>, Aparna Mahadevan<sup>1</sup>, Nhi Nguyen<sup>1</sup>, Hannah Wee<sup>1</sup>, Ashwati Vipin<sup>1</sup>, Tammy Lam<sup>1</sup>, Kai Yi Tay<sup>1</sup>, Jia-Xiang See<sup>1</sup>, Gurveen Sandhu<sup>1</sup>, Yi Jin Leow<sup>1</sup>, Giuseppe D'Agostino<sup>1,9</sup>, Martin Graf<sup>1,2</sup>, Aravind Sivakumar<sup>3</sup>, Sichen Lin<sup>1</sup>, Nguyen Cao Thien Phuc<sup>1</sup>, James Xiao Yuan Chen<sup>1</sup>, Sarah R. Langley<sup>4</sup>, Lay Teng Ang<sup>5,6</sup>, Kyle M. Loh<sup>5,7</sup>, Nagaendran Kandiah<sup>1</sup>, George J. Augustine<sup>1,2</sup> & Christine Cheung<sup>1,3</sup>✉

Vascular dementia is the second most common form of dementia. Yet, the mechanisms by which cerebrovascular damage progresses are insufficiently understood. Here, we create bilateral common carotid artery stenosis in mice, which effectively impairs blood flow to the brain, a major cause of the disease. Through imaging and single-cell transcriptomics of the mouse cortex, we uncover that blood vessel venous cells undergo maladaptive structural changes associated with increased *Epas1* expression and activation of developmental angiogenic pathways. In a human cell model comparing arterial and venous cells, we observe that low-oxygen condition leads to sustained EPAS1 signaling specifically in venous cells. EPAS1 inhibition reduces cerebrovascular abnormalities, microglial activation, and improves markers of cerebral perfusion in vivo. In human subjects, levels of damaged endothelial cells from venous vessels are correlated with white matter injury in the brain and poorer cognitive functions. Together, these findings indicate EPAS1 as a potential therapeutic target to restore cerebrovascular integrity and mitigate neuroinflammation.

Vascular cognitive impairment is a debilitating condition caused by a reduction in cerebral blood flow, that may or may not be associated with a stroke. This affects cognitive abilities such as executive functioning, which results in functional impairment, thereby contributing to vascular dementia<sup>1</sup>. Chronic cerebral hypoperfusion is frequently observed with ageing and leads to progressive changes to brain vasculatures, including greater tortuosity of the arteries, increased

collagen buildup in the veins, and a decline in capillary density<sup>2</sup>. Neuroinflammation has been recognized as a crucial pathological response to cerebral ischemia. However, our understanding of the molecular features of non-neuronal cells, as well as perturbations to the arteriovenous axis in the ischemic brain, remains limited. Endothelial cells maintain the integrity of, and regulate transport across, the blood-brain barrier and control neurovascular coupling<sup>3</sup>.

<sup>1</sup>Neuroscience & Mental Health Program, Lee Kong Chian School of Medicine, Nanyang Technological University, Singapore, Singapore. <sup>2</sup>Temasek Life Sciences Laboratory, 1 Research Link, National University of Singapore, Singapore, Singapore. <sup>3</sup>Institute of Molecular and Cell Biology, Agency for Science, Technology and Research, Singapore, Singapore. <sup>4</sup>School of Biosciences, Cardiff University, Cardiff, UK. <sup>5</sup>Institute for Stem Cell Biology & Regenerative Medicine, Stanford University, Stanford, CA, USA. <sup>6</sup>Department of Urology, Stanford University, Stanford, CA, USA. <sup>7</sup>Department of Developmental Biology, Stanford University, Stanford, CA, USA. <sup>8</sup>Present address: NUS Academy for Healthy Longevity, Yong Loo Lin School of Medicine, National University of Singapore, Singapore, Singapore. <sup>9</sup>Present address: Ochre Bio, Oxford Science Park, Oxford, UK. ✉e-mail: [ccheung@ntu.edu.sg](mailto:ccheung@ntu.edu.sg)

Moreover, endothelial cells interact with and influence surrounding parenchymal tissue on their abluminal side. As such, dysfunctional endothelial cells could have widespread consequences for the brain and serve as an initial driver of vascular cognitive impairment.

Cerebral endothelial cells exist along an arterial-venous transcriptional continuum of gradual phenotypic change along the arteriovenous axis<sup>4</sup>. Neurological diseases arising from vascular pathologies often manifest themselves in a zonation-dependent manner. In cerebral cavernous malformations, loss-of-function mutations in one of the *CCM* genes lead to vascular malformations primarily of venous origin<sup>5</sup>. Similarly, venous endothelial cells are the primary source of endothelial cells in arteriovenous malformations, where misdirected and highly proliferative venous endothelial cells form a direct shunt between arteries and veins, bypassing capillaries<sup>6</sup>. Venous endothelial cells appear as early responders to oxygen changes, with chronic hypoxia inducing endothelial proliferation and vascular leakiness primarily in post-capillary venules, while arterioles show no changes in permeability<sup>7</sup>. Therefore, we hypothesize that intracranial endothelial subtypes differentially affect the zoned patterns of cerebrovascular lesions in chronic cerebral hypoperfusion.

We used a mouse model of chronic cerebral hypoperfusion induced by bilateral carotid artery stenosis (BCAS), which is known to replicate key features of vascular dementia, including white matter changes, blood-brain barrier disruption, and cognitive impairment<sup>8</sup>. Clinical and experimental studies have shown elevated white matter hyperintensities in the frontal lobes of individuals with vascular dementia<sup>9</sup>. Consequently, we focused our vascular phenotyping and single-cell transcriptomics on the prefrontal cortex, a region critical for higher-order cognitive functions such as decision-making, planning, and working memory.

Here, we show that BCAS induces chronic angiogenic sprouting. Further, we show that the endothelial PAS domain protein 1 (*Epas1*), also known as hypoxia-inducible factor 2 alpha (*Hif2α*), is the molecular driver of venous remodeling in vivo, as well as in our in vitro human isogenic arterial and venous cellular system. Rescue experiments in BCAS mice using a small molecule inhibitor of EPAS1 reduce the chronic vascular remodeling, suppress vein-associated microglial activation and restore cerebral blood flow to the level of sham controls. Finally, a blood-based biomarker of circulating damaged endothelial cells (CECs) reveals that venous dysfunction is more pronounced in human subjects with cerebrovascular disease and is correlated with poorer cognitive performance. This work sheds light on the distinct responses of endothelial subtypes to cerebral hypoperfusion and has important implications for targeted vessel normalization strategies to preserve cerebrovascular integrity.

## Results

### Differential arteriovenous responses to cerebral hypoperfusion

Using laser Doppler flowmetry, the baseline cerebral blood flow readings were measured prior to BCAS and sham surgeries in each animal. In the BCAS model, a 0.18 mm (external diameter) microcoil is permanently fixed around both carotid arteries (Fig. 1a). Our longitudinal data quantified relative changes in cerebral blood flow over time, normalized to each animal's baseline measurement, ensuring that our analyses accounted for inter-individual variability in initial flow rates. Immediately following this procedure, cerebral blood flow was reduced to 60–70%, followed by a partial recovery by day 5 that was sustained for up to 30 days post-BCAS (Fig. 1b), reproducing the working model as previously reported<sup>10,11</sup>.

Given that BCAS treatment selectively affects working memory<sup>12</sup>, we focused our cerebrovascular phenotyping on the brain's frontal lobes. Overall vessel density was determined by imaging endothelial cells expressing *Pecam1*. In sham-operated mice, vessel density remained unchanged between day 10 and day 60 post-BCAS (Fig. 1c), indicating vascular stability under normal conditions. In contrast,

BCAS mice exhibited a significant rise in vessel density by day 60, suggesting a gradual response of angiogenesis to chronic hypoperfusion. Frontal lobes largely consist of grey matter, which may be impacted later than white matter<sup>13</sup>, explaining the prolonged angiogenic response. A previous study reported early venous branch growth taking place at 6 days post-BCAS, involving changes in vessel caliber<sup>14</sup>. To study arteriovenous responses to cerebral hypoperfusion, we discerned the origins of FITC-Dextran labeled blood vessels using alpha smooth muscle actin ( $\alpha$ SMA) staining patterns<sup>15,16</sup> to distinguish smooth muscle cell-invested arterial (striated  $\alpha$ SMA) vessels from venous (discontinuous  $\alpha$ SMA) vessels. Indeed, we found that BCAS mice exhibited earlier sprouting of venous vessels compared to sham on day 10 that was sustained till day 60 (Fig. 1d). On the other hand, arterial vessels demonstrated a delayed angiogenic response on day 60. Thus, vascular remodeling under chronic hypoperfusion was characterized by an initial angiogenic response predominantly from venous structures, followed by continued venous expansion and delayed arterial angiogenic adaptation.

Furthermore, in our analysis of vascular lumen size, we focused on anatomically equivalent vascular structures in both BCAS and sham groups - the pericallosal arteries that supply the cingulate cortex, a region within the prefrontal cortex, as well as the sagittal sinus veins that drain the prefrontal cortex. Our results demonstrated that in the BCAS model, veins exhibited significantly increased lumen diameter compared to sham controls, while arteries showed reduced lumen diameter, indicative of constriction on 60 days post-BCAS (Fig. 1e). These findings might suggest compensatory mechanisms in response to chronic hypoperfusion. Arterial constriction reflected the brain's autoregulatory effort to optimize perfusion pressure. On the other hand, venous dilation likely compensated for reduced outflow efficiency, facilitating the drainage of deoxygenated blood.

To discern whether vein lumen changes were due to active vasodilation or passive adjustments in vascular tone secondary to altered intraluminal pressure, we stained brain tissues for endothelial nitric oxide synthase (eNOS). We assessed eNOS protein levels at 60 days post-BCAS, a timepoint representing prolonged cerebral hypoperfusion. We observed increased eNOS protein expression in venous segments, whereas arterial eNOS expression was decreased (Fig. 1f). While eNOS-derived nitric oxide is well known to mediate transient vasodilation in response to acute shear stress, its expression under chronic hypoperfusion may reflect sustained endothelial signaling. To further evaluate structural remodeling, we examined changes in vessel architecture. We observed a significant increase in the wall-to-lumen ratio in veins of BCAS mice (Supplementary Fig. S1a), indicative of venous wall thickening. This was accompanied by elevated collagen IV staining (Supplementary Fig. S1b), suggesting extracellular matrix remodeling. In summary, we found that the cerebrovascular response to hypoperfusion primarily involved venous angiogenic sprouting and vasodilation, highlighting structural and functional adaptations.

### Single-cell transcriptomics reveal pro-angiogenic venous cells

Next, we determined the transcriptomic basis of dysfunctional endothelial subtypes along the arteriovenous axis by examining genome-wide expression changes in endothelial cells. Single-cell transcriptomics was performed on prefrontal cortex tissue obtained from BCAS and sham mice 10 days post-surgery to capture early transcript changes (Fig. 2a). Following quality control filtering (Supplementary Fig. S2a–e) and unsupervised clustering, individual clusters were annotated based on the expression of cell type-specific markers<sup>4</sup>, allowing for the identification of major cell types present in the brain (Fig. 2b). We took particular interest in the endothelial cell population with highly enriched expression of well-known endothelial-specific marker genes, including *Flt1*, *Cldn5* and *Pecam1*. We employed AUCell (v. 1.12.0) to assign individual endothelial cells into distinct subtypes based on expression profiles of arteriovenous

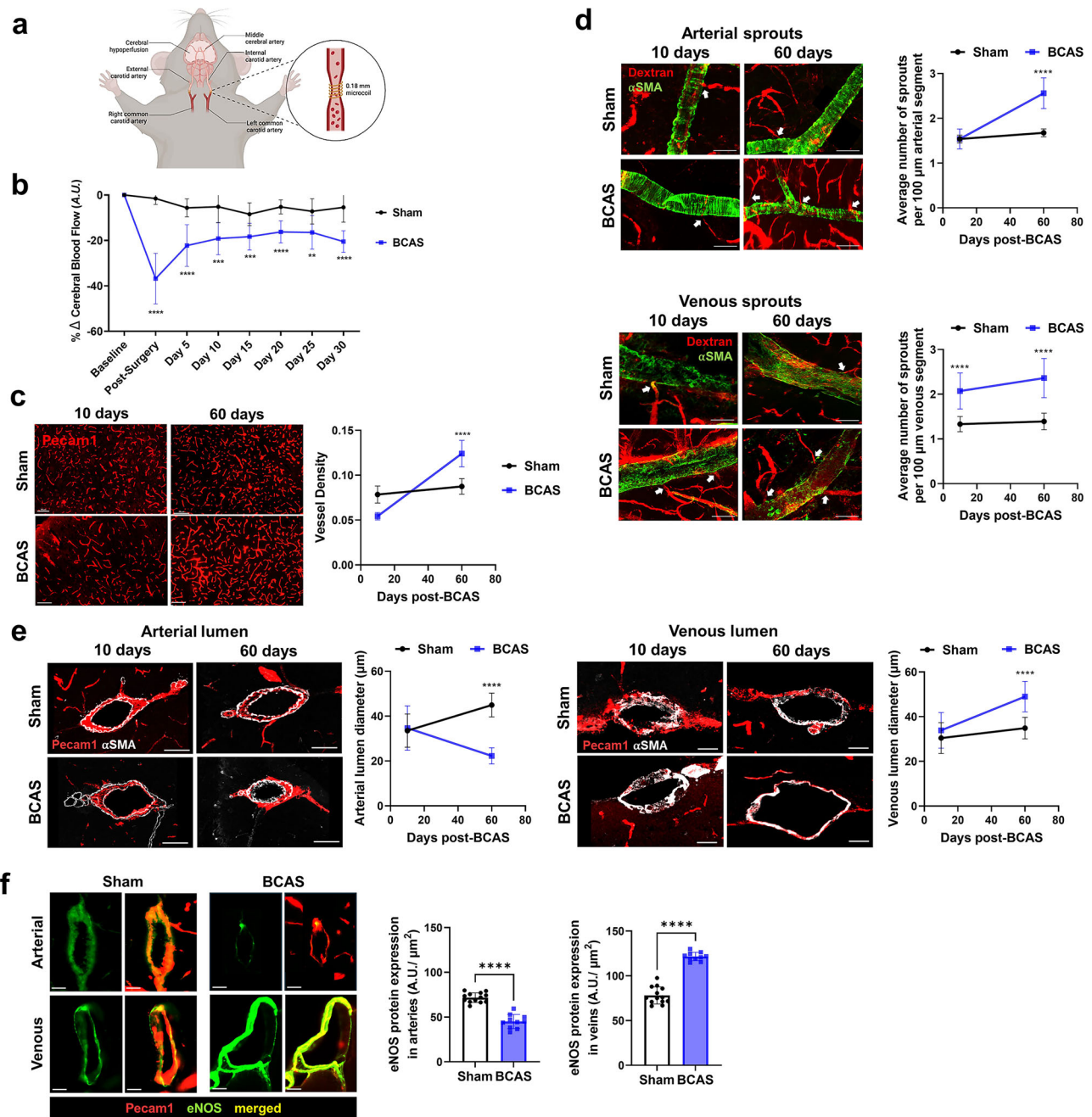


**Fig. 1 | Phenotyping of vessel subtype-specific response to cerebral hypoperfusion.** **a** Schematic of BCAS performed on a mouse. Created in BioRender. Wazny, V. (2025) <https://BioRender.com/ujauv4d>. **b** A time course of percentage of cerebral blood flow changes relative to their respective baseline values of individual mice ( $n = 11$  sham,  $n = 10$  BCAS). Statistical significances reflect differences of sham versus BCAS. **c** Representative immunofluorescence images of Pecam1-positive cerebral vessels (red) acquired 10 days or 60 days post-BCAS surgery. Statistical significances reflect differences of day 10 versus day 60 post-BCAS. Scale bars, 100  $\mu$ m. **d** Three-dimensional images of cerebral vasculatures injected with 500 kDa FITC-conjugated dextran (green). Alpha-smooth muscle actin ( $\alpha$ SMA, green) was used to distinguish arterial (striated) from venous (discontinuous  $\alpha$ SMA) vessels. Quantitative analysis of the number of sprouts per 100  $\mu$ m of vessel length was determined. White arrows indicate angiogenic sprouts. Statistical significances

reflect differences of sham versus BCAS. Scale bars, 30  $\mu$ m. **e** Representative immunofluorescence images of arterial and venous vessels stained with Pecam1 (red) and  $\alpha$ SMA (white) at 10 days and 60 days post-BCAS. Quantitative analysis of the lumen diameter measured by the shortest length across every vessel cross-section. Statistical significances reflect differences of sham versus BCAS. Scale bars, 20  $\mu$ m. **f** Representative immunofluorescence images of eNOS (green) protein expression on Pecam1-positive cerebral vessels (red). Protein expression of eNOS was quantified by eNOS signal intensity per area of the vessel. Statistical significances reflect differences of sham versus BCAS. Scale bars, 20  $\mu$ m. **b–f** Data points represent individual animals in mean  $\pm$  s.d.; unpaired t-test or Mann-Whitney test comparing two groups (two-sided). **c–f** Sample size: 10 days [ $n = 12$  sham (6 females, 6 males),  $n = 10$  BCAS (5 females, 5 males)] or 60 days [ $n = 13$  sham (6 females, 7 males),  $n = 10$  BCAS (5 females, 5 males)]. Source data are provided as a Source Data file.

zonation-dependent genes<sup>4</sup>. This approach identified subpopulations of arterial, capillary, venous-capillary, and venous endothelial cells expressing their respective subtype-specific markers (Fig. 2c). In the proportional analysis of endothelial subtypes,

both sham and BCAS groups exhibited a predominance of cells from small vessels—primarily capillary and venous-capillary endothelial cells—followed by arterial and venous endothelial cells (Fig. 2d). This distribution aligned with the expected proportions of brain



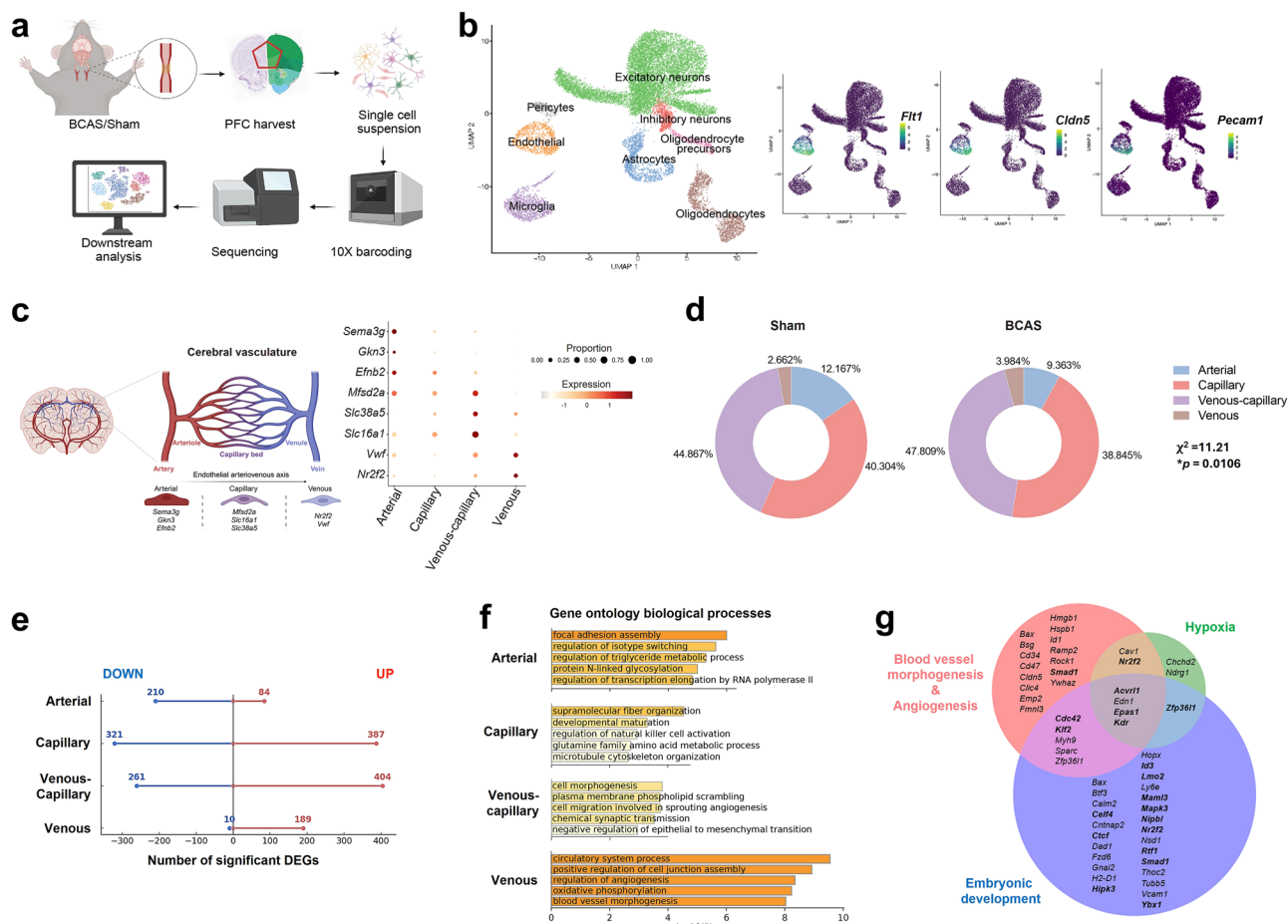


**Fig. 2 | Profiling endothelial cell transcriptomes in response to cerebral hypoperfusion.** **a** Schematic of the single-cell RNA-sequencing workflow on mouse prefrontal cortex. Created in BioRender. Wazny, V. (2025) <https://BioRender.com/g3sc0se>. **b** UMAP visualization of single-cell transcriptomes from BCAS ( $n = 4$ , 2 males, 2 females) and sham ( $n = 4$ , 2 males, 2 females) mouse brains. Expression patterns of endothelial marker genes (*Flt1*, *Cldn5*, *Pecam1*) in dataset have been highlighted on UMAP plots. **c** Endothelial subtypes identified based on gene expression patterns of published curated dataset<sup>4</sup>. Dot plot showing expression and proportion of cells per endothelial subtypes expressing their respective marker genes. Created in BioRender. Wazny, V. (2025) <https://BioRender.com/mSoc7qp>. **d** Proportions of endothelial subtypes obtained from sham versus BCAS groups. Chi-squared goodness-of-fit test (two-sided) was performed to assess the difference in frequencies between the groups.  $\chi^2 = 11.21$ ,  $*p = 0.0106$ . **e** Numbers of significantly upregulated (red lines) and downregulated (blue lines) differentially expressed genes (DEGs) for each endothelial subtype in response to BCAS (adjusted  $p$  value < 0.05, Benjamini-Hochberg method).

Hochberg method). **f** Bar graphs of top 5 enriched gene ontology biological process clusters, based on differentially upregulated genes for each endothelial subtype, sorted by  $p$  value. Terms with a  $p$  value < 0.01, a minimum count of 3, and an enrichment factor > 1.5 (the enrichment factor is the ratio between the observed counts and the counts expected by chance) are collected and grouped into clusters based on their membership similarities. More specifically,  $p$  values are calculated based on the cumulative hypergeometric distribution, and  $q$  values are calculated using the Benjamini-Hochberg procedure to account for multiple testings. Kappa scores are used as the similarity metric when performing hierarchical clustering on the enriched terms, and sub-trees with a similarity of > 0.3 are considered a cluster. The most statistically significant term within a cluster is chosen to represent the cluster. **g** Venn diagram showing the overlap of significantly upregulated DEGs (adjusted  $p$  value < 0.05, Benjamini-Hochberg method) related to various biological processes in BCAS venous endothelial cells. Bolded genes refer to transcription factors.

vasculature<sup>4,17</sup>. Notably, the BCAS group showed a significant increase in the proportion of venous and venous-capillary endothelial cells compared to the sham group. This observation was consistent with phenotypic evidence of more apparent venous angiogenic expansion in BCAS mice (Fig. 1), suggesting endothelial subtype-specific dynamics in brain ischemia.

To investigate the functional relevance of gene expression changes, we performed pseudobulk differential expression analysis to obtain differentially expressed genes (adjusted  $p$  value < 0.05, Benjamini-Hochberg method) in BCAS mice versus sham mice for each of the endothelial subtypes. Among the endothelial subtypes, venous-capillary and capillary cells had the largest number of significant differentially regulated genes (Fig. 2e). Gene ontology (GO) analysis identified top enriched processes across all endothelial subtypes, highlighting vascular structural remodeling in response to cerebral hypoperfusion. These included focal adhesion assembly in arterial

endothelial cells, supramolecular fiber organization in capillary endothelial cells, cell morphogenesis and angiogenesis in venous-capillary endothelial cells, and cell junction assembly and angiogenesis in venous endothelial cells (Fig. 2f). Interestingly, GO analysis also revealed upregulated biological processes related to synapse organization and synaptic signaling across multiple endothelial subtypes (Supplementary Fig. S2f). This finding reflects the organotypic traits of specialized endothelial cells in different tissues, as reported in previous studies<sup>18</sup>. For instance, brain endothelial cells express genes associated with synaptic vesicle function, while heart endothelial cells express cardiac contractile genes. Notably, in the BCAS enriched genes, we observed evidence of endothelial cell de-differentiation, with enriched processes related to blood vessel development in arterial cells, developmental maturation in capillary cells, and embryonic development in venous cells (Supplementary Fig. S2f). This suggests a potential regression to a more plastic or progenitor-like

state, which may contribute to vascular remodeling in response to cerebral hypoperfusion.

To investigate the molecular drivers of venous remodeling in response to cerebral hypoperfusion, we analyzed venous-enriched genes associated with blood vessel morphogenesis, angiogenesis, hypoxia, and embryonic development. The common molecular drivers identified included *Acvrl1*, *Edn1*, *Epas1*, and *Kdr*, with *Epas1* encoding a transcription factor (Fig. 2g). Notably, *Epas1* (also known as *Hif2a*) is a well-established regulator of angiogenesis and could potentially confer venous endothelial cells with heightened sensitivity to hypoxia, promoting their pro-angiogenic phenotype. Further supporting this notion, patients with *EPAS1* gain-of-function mutations exhibit abnormal vascular patterns, including venous dilation, tortuosity, and postcapillary venule leakage<sup>19</sup>. These venous cells also exhibited developmental hallmarks, such as the expression of *Kdr* (vascular endothelial growth factor receptor 2, *Vegfr2*), a known downstream target of *Epas1*<sup>20</sup>.

Since age-related declines in cerebral blood flow are well-documented in humans<sup>21,22</sup>, we examined whether venous endothelial signatures identified in our BCAS model were also evident in the aged brain. We mapped our list of endothelial molecular signatures associated with BCAS onto a published aged mouse brain endothelial single-cell transcriptomic dataset<sup>17</sup>. Notably, we observed upregulation of several key genes implicated in angiogenic and developmental pathways, such as *Epas1*, *Id1*, *Kdr*, *Klf2*, and *Acvrl1*, in aged brain endothelial cells (Supplementary Fig. S2g). These findings suggest a shared endothelial adaptation to cerebral hypoperfusion and vascular aging, involving a reactivation of developmental programs in venous endothelial cells, promoting angiogenic responses. Our current study can advance our understanding of the initial events in vascular cognitive impairment and lay the groundwork for subsequent studies studying aging as a critical modifier of disease trajectory.

As evidenced in Fig. 1, BCAS venous endothelial cells displayed vasoactive properties. We further examined key signaling pathways associated with active vasodilation, specifically focusing on molecules involved in regulating vascular tone, such as nitric oxide, prostacyclin, and G-protein-coupled receptors. This included analyzing genes linked to the eNOS pathway, calcium signaling, and vasodilatory molecules like cyclic GMP. Our analysis showed that, compared to sham control, BCAS condition significantly elevated the expression levels of these vasoactive molecules in venous cells (Supplementary Fig. S2h). This provides insight that venous endothelial cells could be engaged in active vasodilatory responses, in addition to passive adjustments to hemodynamic changes in the BCAS model.

We have made available an interactive browser that allows the exploration of single-cell RNA-seq profiles of BCAS and sham endothelial cells at [https://christinecheunglab.shinyapps.io/mouse\\_bcas\\_ec/](https://christinecheunglab.shinyapps.io/mouse_bcas_ec/).

### EPAS1 preferentially regulates venous angiogenic response to hypoxia

To determine how endothelial cell state could mediate the preferential angiogenic phenotype of venous cells, we leveraged an in vitro system of human arterial and venous cells (Fig. 3a) using an established protocol for endothelial differentiation from human pluripotent stem cells<sup>23</sup>. As most primary endothelial cells lose their subtype specificity after being sub-cultured in vitro, our human arterial and venous endothelial system offered the advantage of isogenic cell subtypes differentiated using chemically defined conditions to drive their subtype commitment. We could reproduce the arterial and venous cell differentiation with high efficiency (~90% arterial and ~80% venous specification; Supplementary Fig. S3). We mapped several venous genes differentially upregulated during BCAS that were associated with angiogenesis, blood vessel morphogenesis and hypoxia onto our single-cell transcriptomes<sup>23</sup> of different stages of human venous differentiation. Expression of most of these genes was enriched in the

pre-venous cell population that is a precursor to venous endothelial cells (Fig. 3b). Therefore, these BCAS-induced genes could potentially represent a dedifferentiated endothelial state, conferring angiogenic capability in venous cells.

To model the differential effects of cerebral hypoperfusion on endothelial subtypes, we subjected both arterial and venous endothelial cells to low oxygen condition (1%) for up to 48 h (Fig. 3a). We acknowledge the absence of glucose deprivation. As the differentiation protocol relied on chemically defined conditions, including glucose in the basal media, removing glucose would disrupt the established protocol and potentially impact differentiation efficiency and cell fate commitment. Therefore, we applied reduced oxygen as the stress paradigm for this model. Because ID1 (also known as Inhibitor of Differentiation 1) maintains multipotency in stem/progenitor cells<sup>24</sup>, we tracked the gene expression of *ID1* in arterial and venous endothelial cells exposed to 1% oxygen. In arterial cells, *ID1* expression levels were sharply induced during the first 2 h of 1% oxygen exposure, and then rapidly declined (Fig. 3c). In contrast, expression of *ID1* in venous cells remained significantly elevated for up to 48 h of exposure to 1% oxygen. A similar reactivation of the developmental program has been documented in the oncofetal reprogramming of endothelial cells during tumor angiogenesis<sup>25</sup>. Our finding highlights the plasticity of venous cells in response to low oxygen and the involvement of developmental genes in chronic angiogenic responses.

Hypoxia-inducible factors play a crucial role in embryonic vascular development. Activation of HIF-1 supports vasculogenesis under intense hypoxic conditions, while the dependence on HIF-2 is essential for the remodeling of newly formed vasculatures<sup>26</sup>. Correspondingly, *Epas1* (*Hif2a*) was significantly upregulated in our BCAS venous population that was actively remodeling. Hence, we compared the dynamics of *EPAS1* induction in human arterial and venous endothelial cells exposed to 1% oxygen. Nuclear translocation of *EPAS1*, a key step in the activation of its downstream hypoxia response genes, was analyzed by measuring colocalization of *EPAS1* with nuclei stained with DAPI (Fig. 3d). *EPAS1* was translocated into the nuclei of venous cells up to 4-fold within 6 h of 1% oxygen exposure and this was sustained up to 48 h (Fig. 3e). On the other hand, induction of *EPAS1* nuclear translocation in arterial cells was milder, reaching 2-fold after 10 h and remaining elevated afterward, albeit at significantly lower levels than observed for venous cells. These expression changes concurred with the temporal regulation of HIFs where *EPAS1* drives chronic hypoxia response (>24 h)<sup>26</sup>.

Iterative structure-based design utilizing the heterodimer of PAS-B domains of *EPAS1* and ARNT lead to the discovery of PT2385 – a potent, selective, and orally active small-molecule inhibitor against *EPAS1*<sup>27</sup>. We performed an endothelial tube formation assay in venous cells and found that 1% oxygen significantly increased the density of tube-like structures in comparison to 21% oxygen (Fig. 3f). Further, the inhibition of *EPAS1* by PT2385 abolished the low oxygen-induced tube formation by venous cells. While 21% O<sub>2</sub> served as a baseline normoxic condition in our study, we recognize that it might not reflect the physiological PO<sub>2</sub> experienced by endothelial cells in vivo, particularly for venous endothelium where PO<sub>2</sub> levels are typically closer to 40 mmHg. Future studies could refine this model by incorporating PO<sub>2</sub> values more reflective of in vivo conditions.

### EPAS1 inhibition restores cerebral blood flow and dampens vein-associated microglial activation

The marked effect of PT2385 in vitro motivated us to examine the actions of this drug in the BCAS model. PT2385 has been used in human clinical trials because of its high penetration of the blood-brain barrier<sup>28</sup>. We hypothesized that *EPAS1* inhibition by PT2385 could reverse venous remodeling induced by cerebral hypoperfusion in vivo. We administered this drug after a 10-day recovery period post-BCAS to allow physiological compensatory angiogenesis to take place (Fig. 4a).

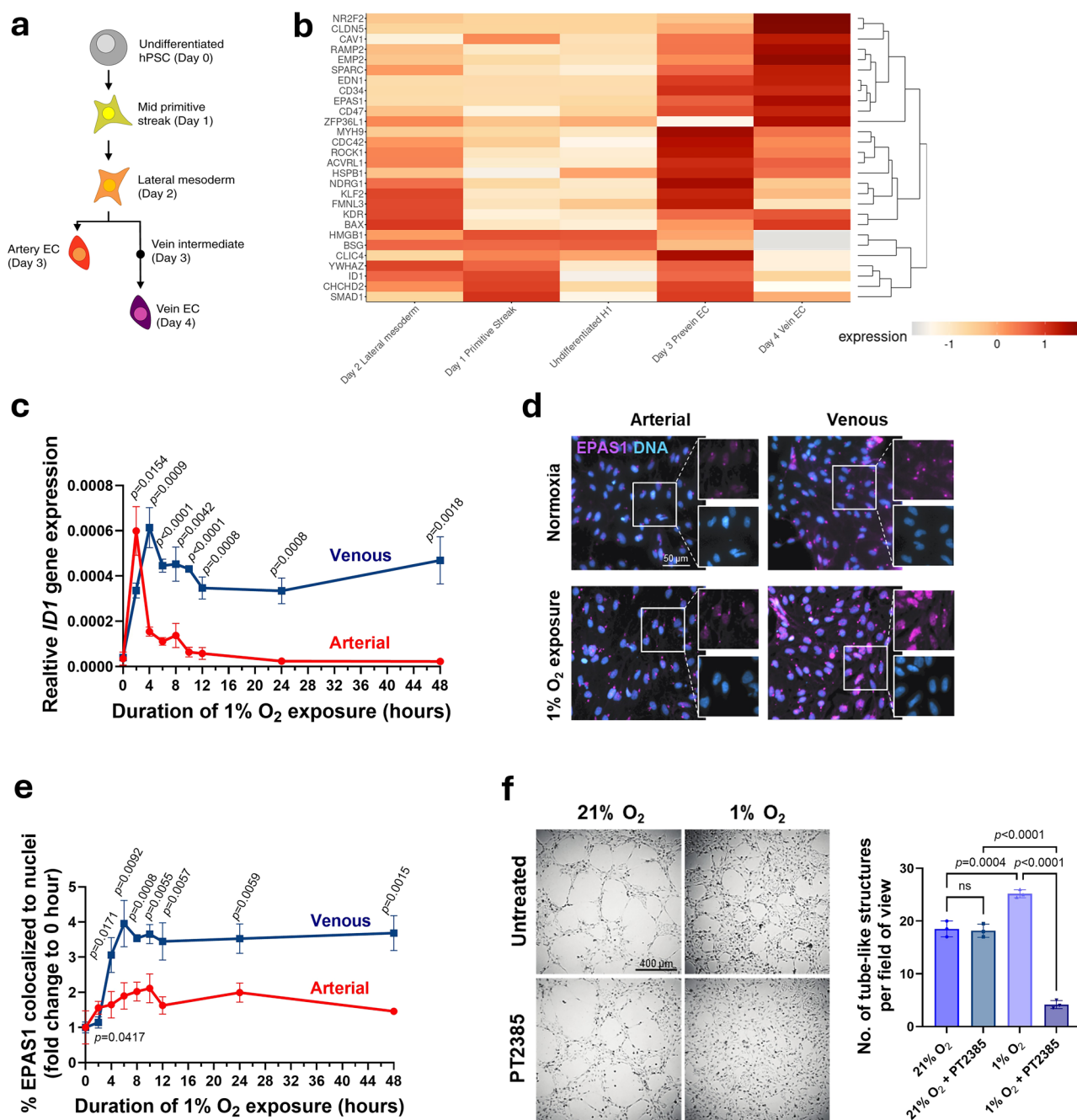


**Fig. 3 | Differential responses of human arterial and venous endothelial cells to 1% oxygen.** **a** Schematic of the endothelial differentiation system. Human pluripotent stem cells were differentiated into primitive streak, then dorsal lateral mesoderm, and subsequently into arterial and venous endothelial cells<sup>23</sup>. **b** Heatmap showing the expression profile of upregulated genes associated with angiogenesis, blood vessel morphogenesis and hypoxia in BCAS venous cells, and mapped onto the single-cell transcriptomics of human pluripotent stem cells, primitive streak, lateral mesoderm, pre-vein, and venous endothelial cell populations. The color intensity indicates the expression level. **c** Time course of relative *ID1* gene expressions comparing arterial and venous endothelial cells under 1% oxygen conditions ( $n = 3$  biological replicates). **d** Representative immunofluorescence

images of arterial and venous endothelial cells stained for EPAS1 (purple) and nuclei (DAPI, blue) in normoxia and after 4 h of 1% oxygen exposure. Scale bar, 50  $\mu\text{m}$ . **e** Quantification of the fold change of % EPAS1 colocalization with the nuclei over time comparing arterial and venous cells ( $n = 3$  biological replicates). **f** Venous endothelial tube formation assay under 21% and 1% oxygen conditions, both untreated and treated with PT2385. Quantification was based on the number of endothelial tube-like structures ( $n = 3$  biological replicates). Scale bar, 400  $\mu\text{m}$ . **c, e, f** Data points represent mean  $\pm$  s.d.; unpaired t-test comparing two independent groups (two-sided), one-way ANOVA for multiple comparisons (two-sided). Source data are provided as a Source Data file.

Mice then received daily doses of PT2385 for 30 days, followed by harvesting of brain frontal lobe tissue to characterize arteriovenous and microglial properties. In BCAS mice, cerebral blood flow was restored to levels comparable to sham controls following PT2385 treatment, whereas cerebral blood flow was significantly reduced in untreated BCAS mice (Fig. 4b). To assay overall cerebrovascular

density, we visualized Pecam1-expressing endothelial structures. Remarkably, the increase in vessel density produced by hypoperfusion in BCAS was reversed back to control levels following PT2385 treatment (Fig. 4c). When we distinguished arterial and venous vessels by co-staining FITC-Dextran labeled vessels with  $\alpha\text{SMA}$ , we found that PT2385 treatment reversed the increased vascular sprouting produced



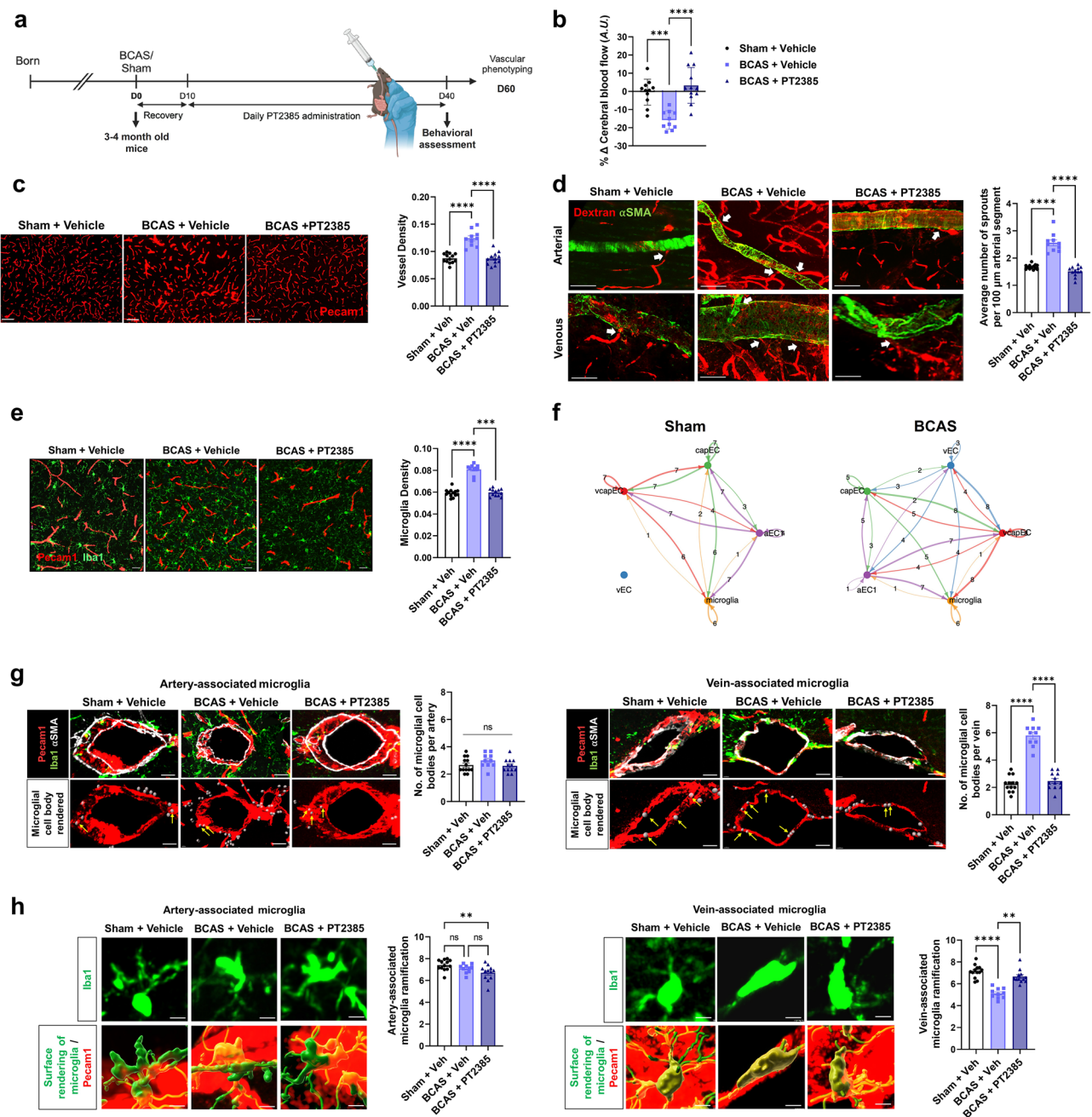


**Fig. 4 | Venous remodeling in response to cerebral hypoperfusion is pharmacologically reversible.** **a** Timeline for BCAS/sham surgery, drug administration, and cerebrovascular phenotyping. Created in BioRender. Wazny, V. (2025) <https://BioRender.com/vm0741>. **b** Percentage of cerebral blood flow changes relative to their respective baseline values of individual mice comparing sham + vehicle ( $n = 11$ ), BCAS + vehicle ( $n = 10$ ), and PT2385-treated BCAS ( $n = 12$ ) mice at 40 days post-BCAS. **c** Representative immunofluorescence images of *Pecam1*-positive cerebral vessels (red) acquired 60 days post-BCAS surgery. Scale bar, 100  $\mu\text{m}$ . **d** Three-dimensional images of cerebral vasculatures injected with 500 kDa FITC-conjugated dextran (green). Alpha-smooth muscle actin ( $\alpha\text{SMA}$ , green) was used to distinguish arterial (striated) from venous (discontinuous  $\alpha\text{SMA}$ ) vessels. Quantitative analysis of the number of sprouts per 100  $\mu\text{m}$  of vessel length was determined. White arrows indicate angiogenic sprouts. Scale bars, 30  $\mu\text{m}$ . **e** Representative immunofluorescence images of microglia stained with *Iba1* (green) against *Pecam1*-positive vessels. Scale bars,

20  $\mu\text{m}$ . **f** Circle plot showing the number of ligand-receptor (L-R) interactions between pairwise cell populations among the endothelial cell subtypes and microglial populations in sham and BCAS groups. aEC arterial, capEC capillary, vcapEC venous capillary, vEC venous endothelial cells. **g** Representative immunofluorescence images of *Iba1*-positive microglia juxtaposed on arterial or venous structures. The average number of microglial cell bodies per vessel (three independent vessels) was measured in every animal, with at least 80% of each rendered spot of microglial cell body colocalizing with the vessels. Yellow arrows indicate examples of vessel-associated microglia. Scale bars, 20  $\mu\text{m}$ . **h** Ramification index of vein- and artery-associated microglia to characterize microglia activation state. Scale bars, 5  $\mu\text{m}$ . **c-e, g, h** Data points represent individual animals in mean  $\pm$  s.d.; one-way ANOVA or Kruskal-Wallis test for multiple comparisons (two-sided). Sample size at 60 days post-BCAS:  $n = 13$  sham + vehicle (6 females, 7 males),  $n = 10$  BCAS + vehicle (5 females, 5 males) and  $n = 12$  BCAS (7 females, 5 males). Source data are provided as a Source Data file.

by BCAS (Fig. 4d). This emphasized the importance of EPAS1 for hypoperfusion-induced angiogenic sprouting.

Disruption of the integrity of cerebrovascular structure by pathophysiological conditions—such as ischemic trauma, brain

tumors, and neurodegenerative diseases—are associated with the accumulation of activated microglia<sup>29</sup>. Similarly, the brains of BCAS mice had a significantly higher density of ionized calcium binding adaptor molecule 1 (*Iba1*)-expressing microglia, an effect that was

eliminated by treatment with PT2385 (Fig. 4e). Analysis of our single-cell data revealed distinct endothelial-microglial communication patterns across endothelial subtypes, shedding light on gliovascular interactions. In the sham control, ligand-receptor interactions were observed between microglia and arterial, capillary, and venous-capillary endothelial cells but were absent with venous endothelial cells (Fig. 4f). Under BCAS conditions, new interactions emerged between venous endothelial cells and microglia, involving *Sema3c-Nrp1/Nrp2/Plxna4*, *Ptn-Ncl*, and *Nampt-Insr* pairs (Supplementary Fig. S4a). Endothelial-derived semaphorin 3 C (Sema3c) likely served as a guidance cue to regulate microglial migration, positioning, and activation, with *Nrp1/Nrp2* and *Plxna4* acting as co-receptors to fine-tune these responses. Similarly, endothelial-derived pleiotrophin (Ptn) might act as a neurotrophic and immunomodulatory factor to modulate microglial activation and phagocytosis through nucleolin (Ncl). The *Nampt-Insr* pair, which is unique to venous endothelial cells, suggest a specialized mechanism where Nampt, an enzyme in NAD<sup>+</sup> biosynthesis, signals through the insulin receptor (Insr) on microglia to regulate energy homeostasis and stress responses.

A growing number of studies have highlighted the involvement of vessel-associated microglia in angiogenesis, vascular maintenance, and potentially the regulation of cerebral blood flow<sup>30</sup>. These microglia are primarily distinguished from parenchymal microglia by their close proximity to blood vessels. To explore the distinct roles of vein- and artery-associated microglia, we assessed their distribution following BCAS. Our analysis revealed that BCAS significantly increased the physical association of microglia with veins, an effect that was attenuated by PT2385 treatment (Fig. 4g, right). In contrast, the levels of microglial association with arteries remained unchanged (Fig. 4g, left). Next, to assess microglial activation, we performed morphological analysis using a ramification index. With this index, long, thin processes yield a high index that reflects resting microglia, while a lower index indicates the more amoeboid shape of activated microglia. Following BCAS, vein-associated microglia showed a significant increase in activation (Fig. 4h, right), whereas artery-associated microglia remained unaffected (Fig. 4h, left). Treatment with PT2385 selectively reduced the activation of vein-associated microglia, suggesting a specific, EPAS1-mediated response of these microglia to BCAS-induced venous stress.

Gene expression analysis revealed that *Epas1* expression in the prefrontal cortex was localized to the endothelial cell cluster, with venous endothelial cells showing a higher relative change in expression compared to other endothelial subtypes (Supplementary Fig. S4b, c). However, *Epas1* expression was negligible in the microglial cluster and was not induced in microglia by the BCAS procedure (Supplementary Fig. S4d). This indicated that EPAS1 inhibition by PT2385 likely reduced microglial activation via venous endothelial-microglial interactions. These findings point to dynamic communication between endothelial cells and microglia, which may play a role in inflammatory responses during brain ischemia. Further studies will be required to understand the mechanisms underlying such interactions.

BCAS impairs spatial working memory, reference memory, and cognitive function<sup>8</sup>. To assess the behavioral impact of PT2385 treatment, we evaluated spatial working memory by using a Y-maze and general locomotor activity in an open field. In the Y-maze, while spontaneous alternations (a measure of working memory) did not differ significantly across groups, the total time taken per alternation pattern was significantly shorter in treated BCAS mice compared to untreated mice (Supplementary Fig. S5a, b). This finding suggests that PT2385 treatment may improve cognitive processing speed or efficiency. In the open field test, the total distance traveled, a measure of general locomotion, remained relatively consistent across all groups (Supplementary Fig. S5c). However, in the analysis of corner zone immobile episodes, a marker of anxiety-like behavior, treated BCAS mice showed a lowered trend and appeared to normalize to sham

control levels (Supplementary Fig. S5d). This suggests that PT2385 may alleviate anxiety-like behaviors.

## Venous dysfunction is associated with human cerebrovascular lesions and poorer cognitive function

Finally, we sought to connect BCAS-related brain venous pathology to cerebral blood flow, cerebrovascular burdens, and cognitive functions in humans. Participants ( $n = 47$ , demographics detailed in Supplementary Table S1) were recruited through the Dementia Research Centre, Singapore, to undergo brain magnetic resonance imaging (MRI), cerebral blood flow analysis, and cognitive assessments (Fig. 5a). The limited availability of primary endothelial cells obtained from patient brain biopsies constituted a bottleneck that we circumvented by using a surrogate biomarker of vascular injury, circulating endothelial cells (CECs). CECs are cells dislodged from damaged endothelia into the bloodstream and serve as a direct indicator of in situ vascular injury or aberrant vascular remodeling. CECs have been validated as a cell-based biomarker for vascular dysfunction across various diseases, including cardiovascular disease, COVID-19, metabolic disorders, preeclampsia, and sickle cell anemia<sup>31</sup>. Thus, blood was collected from every subject and then processed to retrieve the peripheral blood mononuclear cell (PBMC) fraction. CECs were then detected in PBMC samples by flow cytometry using a combined immunophenotypic profile of CD45/CD31<sup>+</sup>/CD133/DNA<sup>+</sup> (Fig. 5a).

MRI white matter hyperintensity, a measure of cerebrovascular disease, was quantified by a modified Fazekas scale<sup>32,33</sup>. White matter hyperintensity was measured in four brain regions: right periventricular, left periventricular, right deep subcortical, and left deep subcortical. Absent-to-mild cerebrovascular disease was defined as a score ranging from 0–4 on the total Fazekas scale, whereas individuals with scores of 5–12 were classified as having moderate-to-severe cerebrovascular disease. Visual ratings were carried out independently by two trained raters, and any substantial discrepancies in scores were resolved through consensus. To measure cerebral perfusion, cerebral blood flow was determined by 2D pulsed arterial spin labeling data from brain MRI images<sup>34</sup>.

Participants with mild cerebrovascular disease (Fazekas score 1–4) exhibited a significant inverse correlation between the number of CECs and cerebral perfusion (Fig. 5b), indicating a decline of cerebral blood flow is associated with endothelial damage. However, this trend was only apparent in the absent-to-mild cerebrovascular disease groups (Fazekas score 0–4), rather than in severe cerebrovascular disease (Fazekas score  $\geq 5$ ). This suggests that cerebral hypoperfusion gave rise to early vascular perturbations. In cases of severe white matter lesions, factors such as neuronal deficits, glial dysfunction, and neuroinflammation may have confounded the correlation between cerebral perfusion and endothelial changes.

To identify the subset of CECs originating from venous structures, we required an additional marker that fulfilled both organotypic signature and venous subtype of interest. To find a marker of venous endothelial cells, we leveraged advances in single-cell transcriptomics by mining a single-cell transcriptomic atlas of organotypic endothelial cells isolated from 11 mouse tissues<sup>35</sup> (Supplementary Fig. S6a). Expression of *atypical chemokine receptor-1* (*Ackr1*) demonstrated enriched venous expression in the brain, soleus muscle, extensor digitorum longus muscle, intestines, and liver. This is consistent with the venous specificity of *ACKR1* expression in human brain single-nucleus transcriptomes<sup>36,37</sup> (Supplementary Fig. S6b). We recognized that *ACKR1* protein might not be exclusively expressed in brain endothelial cells or venules; hence more precise markers for selective identification of damaged venous cells in the brain would be desirable. Nonetheless, we used *ACKR1* expression to identify damaged CECs that originated from venous vessels (Fig. 5a). When the human subjects were divided into two groups based on the presence (Fazekas score  $> 0$ ) or absence (Fazekas score = 0) of cerebrovascular disease, there was



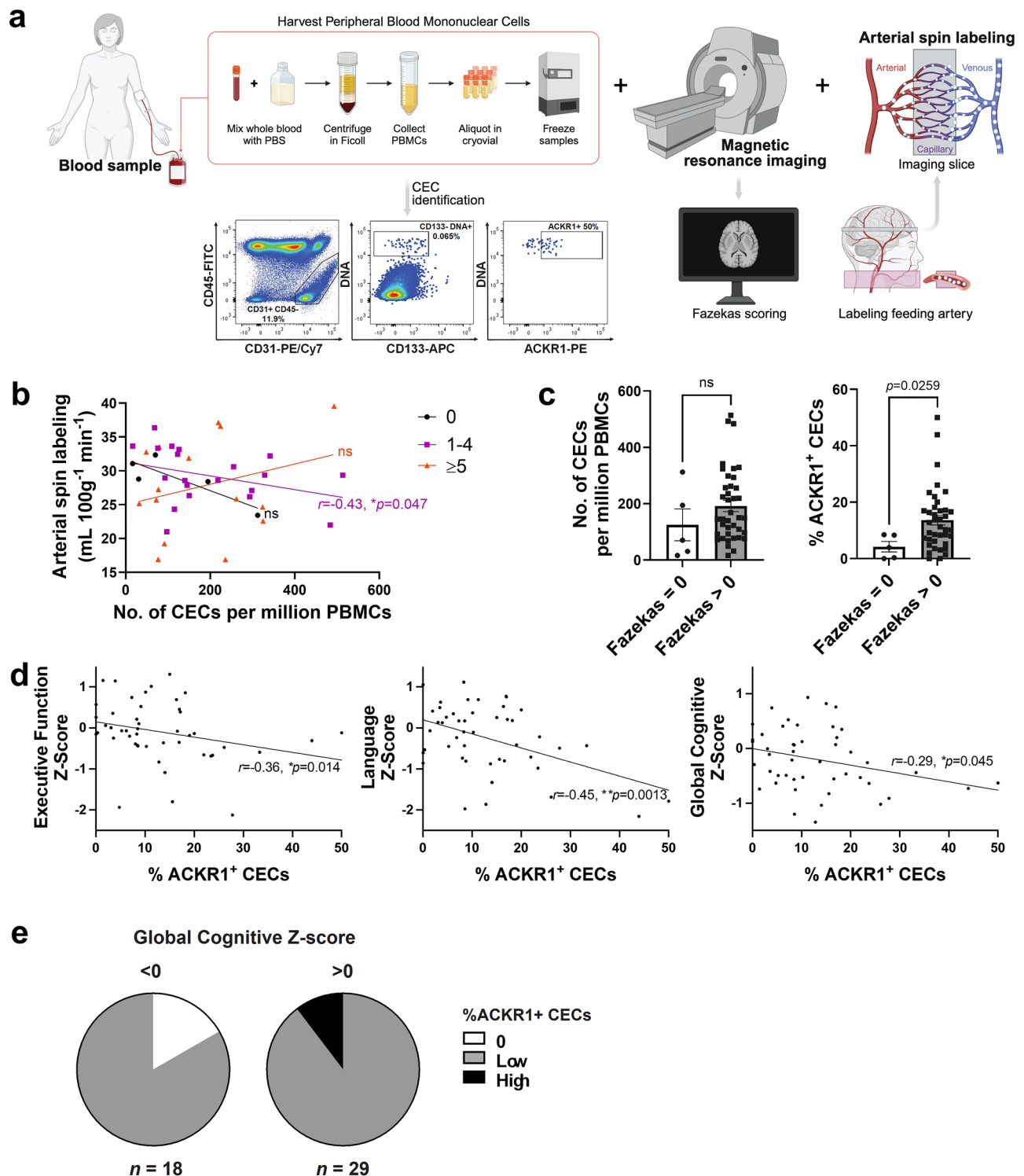


**Fig. 5 | Circulating venous endothelial cell levels are elevated in human subjects with cerebrovascular disease burden.** **a** Schematic of study workflow. Human subjects underwent blood sample collection, magnetic resonance imaging and arterial spin labeling. Flow cytometry analysis on peripheral blood mononuclear cells (PBMCs) was used to identify circulating endothelial cells (CECs) based on the immunophenotypic markers of CD45<sup>+</sup>/CD31<sup>+</sup>/CD133<sup>+</sup>/DNA<sup>+</sup>, followed by characterization with brain venous marker, ACKR1. Created in BioRender. Wazny, V. (2025) <https://BioRender.com/9ypd05j>. **b** Spearman's correlation analysis between cerebral tissue perfusion, measured by arterial spin labeling, with the number of CECs per million PBMCs. Subjects were grouped by Fazekas scores. Spearman's correlation coefficient  $r$  and  $p$  values (two-tailed test) are indicated. **c** Quantification of the

number of CECs per million PBMCs (left), and percentage of ACKR1<sup>+</sup> CECs (right) in subjects grouped by presence (Fazekas > 0,  $n = 39$  individual participants) or absence (Fazekas = 0,  $n = 5$  individual participants) of cerebrovascular disease burden. Data points represent mean  $\pm$  s.e.m.; Mann-Whitney test (two-sided);  $*p < 0.05$  and ns non-significant. **d** Correlation analysis between the percentage of ACKR1<sup>+</sup> CECs and Z-scores of various cognitive functions. Spearman's correlation coefficient  $r$  and  $p$  values (two-tailed test) are indicated for executive function Z-scores. Pearson's correlation coefficient  $r$  and  $p$  values (two-tailed) are indicated for language and global cognitive Z-scores. **e** Proportional analysis of zero (0), low (< 95<sup>th</sup> percentile), and high (> 95<sup>th</sup> percentile) percentages of ACKR1<sup>+</sup> CECs in subjects grouped by negative and positive global cognitive Z-scores. Source data are provided as a Source Data file.

an upward trend in CEC levels (Fig. 5c, left), and a significant increase in the percentage of ACKR1<sup>+</sup> CECs in subjects with cerebrovascular disease (Fig. 5c, right). Hence, white matter lesions seen in patients with vascular cognitive impairment might be associated with venous dysfunction.

Increases in white matter hyperintensity and cerebrovascular burden are associated with poorer cognition<sup>34</sup>. In our subject cohort, the levels of ACKR1<sup>+</sup> CECs were correlated with decreases in cognitive performance, particularly in executive function and language skills (Fig. 5d). In neuropsychological examinations, both single test scores and entire performance profiles can be used to identify cognitive deficits<sup>38</sup>. We further derived an average global cognitive score – based on executive function, language, visuospatial, episodic memory abilities, and processing speed – to compare to CEC biomarkers. A significant correlation was observed between a higher percentage of ACKR1<sup>+</sup> CECs and a decrease in global cognition (Fig. 5d). When the subjects were subset according to zero, low or high (>95<sup>th</sup> percentile) percentage of ACKR1<sup>+</sup> CECs, individuals with less than average global cognitive performance (negative Z-score) sustained greater proportion of detectable ACKR1<sup>+</sup> CECs, especially ‘high’ levels of ACKR1<sup>+</sup> CECs (Fig. 5e). Taken together, we conclude that venous endothelial damage was associated with poorer cognitive functions in humans.

In human genetic studies of cognitive performance, the intergenic single nucleotide polymorphism rs34743896 has been associated with a change in attention score<sup>39</sup>. Interestingly, the closest gene to rs34743896 is *EPAS1* (~30 kb away). We performed data mining of in situ Hi-C sequencing datasets that map genome-wide chromatin contacts in human umbilical vein endothelial cells<sup>40</sup>, human aortic endothelial cells<sup>41</sup>, and human brain prefrontal cortex<sup>42</sup> (Supplementary Fig. S7). Given the proximity of rs34743896 and *EPAS1*, both were indeed found in regions of intensified chromatin interactions, and potentially within the same topographically associating domains. While it is known that genetic variants can act distally, to affect regulatory elements of genes within the same topographically associating domains where regions of chromatin physically interact more frequently, further investigation is required to define the relationship between *EPAS1* and cognition.

## Discussion

Our study delineated the responses of specific subtypes of endothelial cells to cerebral hypoperfusion at the molecular, structural, and functional levels. We pinpointed cross-species convergence of pathways in venous susceptibility to cerebral hypoperfusion in a clinically relevant BCAS mouse model of vascular dementia, as well as in deeply phenotyped human subjects. Our human analyses linked hallmarks of venous endothelial dysfunction to the risk of cognitive impairment. In line with our observations in the BCAS mouse model, the well-described loss of blood-brain barrier integrity seen in cerebral hypoperfusion<sup>43,44</sup> and inflammatory demyelinating diseases<sup>45</sup> have been related to venular leakiness and venous association with leukocyte infiltration. Our findings also suggest that venous normalization could be a therapeutic strategy to moderate vein-associated microglial activation and potentially reduce neuroinflammation in brain ischemia.

Emerging data suggest that venous endothelial cells are unique in their ability to serve as the primary source of endothelial cellular mass during both developmental and pathological angiogenesis<sup>46</sup>. During assembly of the vascular network within the zebrafish hindbrain, the arterial system is predominantly derived from the sprouting and migration of endothelial cells from pre-existing veins<sup>47,48</sup>. Similarly, in mouse embryonic development, widespread capillary arterialization occurs from venous-features plexus during the expansion of intra-embryonic vasculatures<sup>49</sup>. During postnatal vascular development of the mouse retina of neural crest origin, endothelial tip cells that are derived from veins differentiate into other endothelial subtypes<sup>6,50</sup>.

Such developmental plasticity of venous cells appears to translate to an angiogenic phenotype in diseases of the brain. Here, the molecular signatures of BCAS venous cells matched the dedifferentiated characteristics of venous precursor cells in a human endothelial differentiation system<sup>23</sup>. Angiogenic endothelial subpopulations have also been commonly identified in the human brain single-cell transcriptomes of arteriovenous malformations<sup>51</sup> and Alzheimer’s disease patients<sup>52</sup>, harboring pathological hallmarks for angiogenesis and immune cell reactivity respectively. We believe that venous endothelial cells exhibit a propensity for reactivation of their developmental programs, leading to chronic vascular remodeling and subsequent cerebrovascular instability.

*EPAS1* plays both essential and pathophysiological roles in angiogenesis and vascular remodeling<sup>53</sup>. *Epas1*-deficient mouse embryos develop severe vascular defects and die in utero<sup>54</sup>. While blood vessels in these mice are formed by vasculogenesis, they either fuse improperly or fail to assemble into larger vessels, suggesting that *EPAS1* plays an important role at post-vasculogenesis stages and is required for the remodeling of the primary vascular network into a mature hierarchy pattern. Here, we uncovered that *EPAS1* (HIF-2 $\alpha$ ) could be a key driver of preferential venous remodeling. Human venous endothelial cells, when subjected to low oxygen (1%) condition in vitro, responded with more pronounced and sustained *EPAS1* signaling, unlike the arterial endothelial cells. Both ID1 and *EPAS1* revealed similar expression dynamics in venous endothelial cells under low oxygen conditions. *Id1* is highly expressed in the endothelial cells of developing vessels and tumor vasculatures, and the knock-out of *Id1* results in embryonic lethality due to vascular malformations and premature neuronal differentiation<sup>55</sup>. *ID1* encodes a helix-loop-helix (HLH) protein devoid of DNA binding activity but can inhibit the DNA binding and transcriptional activation ability of the proteins it interacts with. While the direct interaction between ID1 and *EPAS1* is unknown, a close member of the HLH family, ID2, can interact with the von Hippel-Lindau (VHL) ubiquitin ligase complex, consequently inhibiting the ubiquitylation and degradation of *EPAS1*<sup>56</sup>. Regarding the more well-studied HIF-1 $\alpha$ , ID1 protein enhances its protein stability through reduced association of VHL with HIF-1 $\alpha$ , thus interfering with proteasomal degradation of HIF-1 $\alpha$ <sup>57</sup>. In fact, *EPAS1* and HIF-1 $\alpha$  share a 48% amino acid sequence identity and possess similar protein structures. Despite their unique regulatory pathways, both proteins undergo oxygen-dependent degradation facilitated by VHL, highlighting a common regulatory mechanism<sup>26</sup>. Therefore, it would be intriguing to speculate that the interplay between ID1 and *EPAS1* might be facilitated via ID1’s interaction with VHL, underscoring the need for further investigation.

To understand whether venous response is adaptive or maladaptive under blood flow impairment, we believe that *Epas1* could initially drive compensatory angiogenesis from venous endothelial cells. We have observed arterial constriction to regulate flow and venous dilation to manage outflow, highlighting the hemodynamic implications of cerebrovascular responses to hypoperfusion. Unlike HIF-1 that controls acute response to hypoxia, *EPAS1* mediates chronic responses<sup>26</sup>. Hence, sustained imbalances of arteriovenous responses in brain ischemia could transition to maladaptation. While venous pathology has not been known to directly cause chronic hypoperfusion, the absence of valves in cerebral veins permits bidirectional blood flow, potentially exacerbating blood outflow. Hence, venous cells would be exposed to more metabolic by-products due to impaired drainage, exacerbating vascular remodeling. Elevated CEC levels in human subjects, correlated with reduced cerebral blood flow and cognitive impairment, could indicate endothelial cells that have been shed from dysfunctional blood vessels, often because of endothelial damage or stress. This underscores the need for therapeutic interventions to alleviate venous dysfunction and restore cerebral

blood flow. Given the temporal dynamics of EPAS1 in driving chronic hypoxia response, an effective therapeutic approach targeting EPAS1 would require precise timing and further research of its stage-specific effects on different cell types.

Our finding of venous dependency on EPAS1-driven angiogenesis draws parallels with a gain-of-function *EPAS1* mutation in human patients, which results in a spectrum of venous anomalies and malformations that are attributed to failure of developmental vascular regression<sup>19,58</sup>. A mutation in the oxygen degradation domain of EPAS1 hinders its hydroxylation by prolyl hydroxylase domain-containing protein 2 and its subsequent binding to the VHL protein. This leads to stabilization of EPAS1 and lack of response to increasing oxygen tension. EPAS1 stability, in turn, contributes to chronic venous remodeling. Interestingly, genetic adaptations involving EPAS1 in high-altitude populations, notably in Tibetan and Andean highlanders, reduce hypoxia-induced responses such as excessive erythrocytosis, which can strain the cardiovascular system<sup>59,60</sup>. In Tibetans, EPAS1 adaptations, mainly missense mutations and regulatory changes, moderate the hypoxia response, preventing extreme red blood cell increases and likely supporting cognitive stability through consistent cerebral oxygenation. Conversely, Andeans, who have adaptations that result in higher hematocrit levels, may experience a greater risk of hypoxia-related complications, including potential subtle cognitive effects with prolonged altitude exposure. These differences highlight how EPAS1 adaptations contribute to resilience against low oxygen but suggest that cognitive outcomes are likely shaped by other genetic and environmental factors. Further studies on EPAS1's role in cerebrovascular and cognitive resilience at high altitudes could provide valuable insights, especially concerning hypoxia-related cognitive effects in lowland populations.

Developing therapeutic interventions targeting venous maladaptation to low oxygen, as well as neuroinflammation, will be beneficial. Our study demonstrated that inhibiting EPAS1 through a small molecule drug, PT2385, effectively reversed the venous response to low oxygen, both in vitro and in vivo, and specifically reduced the density and activation of vein-associated microglia. Vessel-associated microglia appear to play a role in cerebral blood flow regulation during hypoperfusion. Microglial P2RY12 contributes to cerebrovascular adaptation during common carotid artery occlusion, and its blockade reduces cerebral blood flow without affecting neuronal responses<sup>61</sup>. The microglial processes around capillaries correlate with cerebral blood flow levels during transient ischemia<sup>62</sup>, in turn indicating blood flow's role in microglial activation. In systemic inflammation, microglia migrate towards cerebral vessels to initially protect their integrity, then transform into a reactive state that results in widespread neuroinflammation<sup>63</sup>. In vitro evidence further suggests that damaged endothelium can promote microglia to transition toward an inflammatory phenotype<sup>64</sup>. Thus, decreased vein-associated microglial density and activation following PT2385 treatment here may be attributable to the resolution of venous dysfunction and impaired blood flow. However, we recognize a conundrum with the direct effect of EPAS1 inhibition on microglia. Blocking Cav2.2 channels has been shown to enhance microglia towards a neuroprotective state involving EPAS1 activation<sup>65</sup>. Given the potential neuroprotective role of EPAS1 in microglia, targeted drug delivery to normalize venous remodeling will be important.

Our study bridges findings from animal models to human conditions, aligning cerebrovascular and cognitive parameters where feasible. In mice, cerebral blood flow was quantified using Doppler flowmetry, providing real-time measurement of blood flow changes. For human subjects, MRI arterial spin labeling was employed, offering a non-invasive assessment of cerebral perfusion. Although distinct methods, both techniques allow us to infer cerebral blood flow, enabling meaningful cross-species comparison of perfusion dynamics.

In terms of cerebrovascular phenotyping, in vivo analysis of cerebrovascular structure in our mouse model included quantitative measurements of sprouting and vasodilation in arteriovenous vessels, markers directly relevant to vascular remodeling and endothelial function. In humans, MRI imaging of white matter hyperintensities serves as an indirect marker of small vessel disease. To assess cognitive function and its relation to vascular changes, we performed behavioral tests in mice, focusing on working memory and motor function, which approximate the executive function, language, and memory assessments conducted in our human cohort. Our approach aims to achieve an integrative, cross-species analysis; however, we highlight some inherent difficulties in aligning functional measures across species. Differences in the pathogenesis between mice and humans pose challenges in direct comparisons. Specific markers of vascular integrity that are readily obtainable in the mouse model cannot be directly measured in human subjects. In our human cohort, we utilized a composite cognitive score, derived from assessments with distinct testing formats, to approximate functional domains close to those evaluated in mouse behavioral tests.

We have noted the following limitations in our study. While the brain pathologies in BCAS mice share similarities with those in human subcortical ischemic vascular dementia, the model does not exhibit arteriosclerosis because hypoperfusion is induced through the occlusion of extracranial vessels<sup>8</sup>. This highlights a key difference between the mechanisms of hypoperfusion in human cerebral small vessel disease and the BCAS model. We acknowledge that cerebral blood flow reduction in BCAS occurs rather acutely due to the placement of microcoils, instead of over a long time, as seen in atherosclerosis, which may allow time for collateral vessel formation. However, BCAS still induced chronic hypoperfusion, with blood flow not returning to baseline levels over a 30-day period in our data. Alternative methods that achieve a more gradual reduction in cerebral blood flow, such as amyloid-based constrictors or hypercholesterolemic models that develop atherosclerosis, could be considered<sup>66</sup>. To address the inherent limitation of laser-Doppler flowmetry in providing only relative perfusion readings, complementary imaging modalities, such as magnetic resonance arterial spin labeling (MR-ASL), are more appropriate for quantifying absolute cerebral blood flow (e.g., in ml/min/100 g). As such, MR-ASL would be necessary to draw definitive conclusions on absolute perfusion levels and should be considered in future studies to extend our findings.

In conclusion, targeting EPAS1 as a therapeutic strategy for vascular normalization could slow the progression of cerebrovascular disease. EPAS1 inhibition mitigated vascular remodeling and dampened vein-associated microglial activation in our BCAS model, suggesting that modulating chronic angiogenesis might have a role in reducing neuroinflammation. Currently, diagnosis of vascular dementia relies on neuroimaging and assessment of cognitive function impairment<sup>67,68</sup>. With this criterion, however, patients are only diagnosed after the onset of cognitive decline when the disease is irrevocably developed, as there is yet no effective treatment. Our analysis of patient CECs, as part of a minimally invasive routine blood test, will translate to accurate and transferable endpoints in early clinical assessment of vascular health. The proof-of-concept in correlating the levels of CECs with cognitive functions in patients may have applications in stratification-based clinical trials for selecting patients for vascular-protective therapy, and as treatment-prediction biomarkers to interpret clinical trial findings mechanistically.

## Methods

### Human studies approval, subject enrolment, and sample collection

This study was approved by the Local Ethics Committee, namely Nanyang Technological University Institutional Review Board (IRB-2021-1036). Each participant provided written informed consent after



being informed about the study's nature and potential consequences. The study protocol is in accordance with the Helsinki Declaration. Human subjects were recruited as part of the Biomarkers and Cognition Study, Singapore (BIOCIS)<sup>69</sup> of Dementia Research Centre Singapore. Baseline patient characteristics, comprising age, sex, ethnicity, and comorbidities, were collected through blood sampling at the time of enrolment (Supplementary Table S1). For blood sample collection, 6–8 mL was collected from each participant via venepuncture and processed in the lab within 3 h. Following Ficoll centrifugation of fresh blood, buffy coat layers containing PBMCs were isolated for analysis of circulating endothelial cells.

### Animal studies approval and BCAS procedure

BCAS surgery was performed by a skilled animal surgeon according to published protocol<sup>10</sup>. C57BL/6J mice (aged 3–4 months) were anesthetized with 2.0% isoflurane before a midline cervical incision was made for tissue harvesting at 10 or 60 days post-BCAS. Common carotid arteries were exposed by careful separation of tissue layers and the vagal nerves. 0.18 mm diameter microcoils (Sawane Spring Co., Ltd) were applied by rotating them around each common carotid artery. Body temperature was monitored and kept within the range of 36.5–37.5 °C by using a heating blanket. After microcoil application, the incision was closed with a silk suture, and mice were left on the heating blanket after surgery. Sham mice underwent the same procedure without microcoil placement. Four sham and 4 BCAS mice (2 males and 2 females per experimental group) were used for transcriptomic studies. For histological and functional studies, 10–13 mice were used per experimental group with both sex representations.

Care provided to the animals followed institutional guidelines and was approved by the local Institutional Animal Care and Use Committee (IACUC # A18095). Animals are housed in individually ventilated cages on forced ventilation-based system, air is HEPA filtered for supply to IVC cages, and HEPA filtered on exhaust. Exhaust air is not recycled. Room air change per hour set to >10. Animal holding room temperature is set at 22 °C (+/- 2 °C), with humidity kept in 50% to 70% range. Holding rooms have surface mounted and water-resistant lighting fixtures, set to provide 12:12 hrs photoperiod (light:dark). Housing density follows the NACLAR guidelines. Animals are fed standard irradiated maintenance or breeding rodent diets. Water is supplied by standard water bottles. All animals are housed on autoclaved corn cob bedding and are provided with nesting material. Environmental enrichment program and strict social housing practice is in place.

### Measurement of cerebral blood flow by laser-Doppler flowmetry

Under deep anesthesia (2% v/v isoflurane), a 1 cm midline scalp incision was made and retracted to expose the skull. A laser Doppler flowmetry probe (FLO-N1, OMEGAWAVE, Inc.) was carefully positioned at the midpoint between bregma and lambda over the parietal cortex, a location that does not directly overlay large arterial or venous structures. A 3 mW, 780 nm laser was delivered through the probe to record cerebral blood flow. Baseline cerebral blood flow was recorded at the onset of surgery, following anesthesia induction. Probe positioning was standardized across animals, and the signal was allowed to stabilize within  $\pm 0.5$  perfusion units before data collection. In each animal at every time point, three replicate readings were acquired and averaged to ensure consistency. Subsequent cerebral blood flow readings were taken after microcoil implantation and at regular intervals, every 5 days up to day 30, or on day 40 for drug treatment studies. Cerebral blood flow values were expressed as a percentage of each animal's individual baseline. To minimize variability, physiological and environmental conditions were tightly controlled. Mice were maintained at  $37 \pm 0.5$  °C using a feedback-regulated heating pad. All measurements were

performed in a thermostat-controlled, windowless room with constant artificial lighting.

### Histological analysis by immunofluorescence staining

Mice were deeply anesthetized with an intraperitoneal injection of ketamine (100 mg/kg) and xylazine (10 mg/kg), and transcardially perfused with DPBS (SH3002803, Hyclone). Cerebral tissue was fixed in 4% paraformaldehyde (PFA; 09154-85, Nacalai Tesque) overnight at 4 °C. The anterior 4 mm portion of the brain was cryoprotected in 30% (w/v) sucrose solution (Thermo Fisher Scientific, 57-50-1), embedded in Tissue-Tek optimal cutting temperature compound (Sakura, 4583), and flash frozen in liquid nitrogen. Coronal sections of 20  $\mu$ m thickness were cut on a cryostat (Leica, CM3050 S) and mounted on glass slides. The slides were washed with DPBS, permeabilized with 0.1% Triton X-100 (omitted for CD45 staining), and blocked with 1% bovine serum albumin (BSA; 9998, Cell Signaling Technology). Primary antibody incubations were done overnight at 4 °C. The slides were then washed and incubated with fluorophore-conjugated secondary antibodies for 1 h at room temperature in the dark. Sections were counter-stained with DAPI (1:5000) and mounted using Fluoromount Aqueous Mounting Medium (Sigma-Aldrich, F4680). Antibody details are provided in Supplementary Table S2.

To discern the origins of endothelial cells in the expansion of the vascular network, we used  $\alpha$ SMA staining patterns<sup>15,16</sup> to distinguish smooth muscle cell-invested arterial (striated  $\alpha$ SMA) vessels from venous (discontinuous  $\alpha$ SMA) vessels. For lumen diameter analysis, we implemented a systematic approach to identify and consistently measure vessels of the same type across samples. Specifically, we focused on the pericallosal artery and vein, which supply the cingulate cortex—a region within the prefrontal cortex—allowing us to compare analogous vascular structures in both BCAS and sham groups. This approach minimized variance by avoiding misidentification between small veins and arterioles, which could otherwise introduce confounding factors. To characterize active vascular remodeling, we derived wall-to-lumen ratio<sup>70</sup> to determine structural changes due to wall thickening.

### Histological analysis by three-dimensional vascular visualization

Mice were transcardially perfused with DPBS, followed by 50 mg/mL 500 kDa FITC-Dextran (Sigma-Aldrich, FD500S). Brains were harvested and fixed in 4% PFA overnight at 4 °C. Subsequently, the prefrontal cortex tissue was used for tissue clearing. Pre-delipidation was done using 50% CUBIC-L (TCI, T3740) for 3 h at room temperature, followed by further delipidation with CUBIC-L at 37 °C for 5 days until optical transparency was achieved. CUBIC-L was refreshed on days 1 and 2, followed by every other subsequent day. The tissue was washed with DPBS, permeabilized with 0.2% Triton X-100, and then blocked with 5% BSA. Incubation with conjugated-primary antibodies was done at 4 °C for 5 days. Tissue was then washed and stored in DPBS at 4 °C until imaging. Antibody details are provided in Supplementary Table S2.

### Image acquisition and analysis

High-resolution images of alpha smooth muscle, microglia and arterial/venous sprouting from 1 mm thick brain slices were acquired using the inverted laser scanning confocal with Airy scan super-resolution capability (LSM800, ZEISS) at NTU-Optical Bio-Imaging Centre (NOBIC). High-throughput imaging of multiple prefrontal 20  $\mu$ m brain sections for vascular density and eNOS was carried out the Carl Zeiss Axio Scan.Z1 slide scanner. Other images were acquired using the inverted widefield fluorescence microscope (CellDiscoverer7, ZEISS). Multi-channel images were captured using the ZEN software (Blue Edition, Carl Zeiss). Imaris (v 9.9.1), ImageJ2 (v 2.14.0) and MatLab (R2023b) were used in the processing, analysis and quantification of images.

## 1. Microglial ramification analysis

### a. Image Preprocessing and Analysis

Quantitative analysis of microglial association with vessels was performed using a custom MATLAB-based pipeline, designed for automated processing and extraction of microglial connectivity features. The pipeline included the following steps:

### b. Input Image Acquisition: “.tif” images containing immunolabeled microglia and vessels were loaded into the pipeline. Each image was pre-assigned to its respective experimental group (BCAS SHAM, BCAS Vehicle, or BCAS Drug) and vessel type (artery, vein, micro vessel).

### c. Microglial Connectivity Analysis:

The green channel (corresponding to microglial labelling) was extracted from each image. Noise was reduced using a median filter, and microglial structures were enhanced using a Frangi vesselness filter for better detection of curvilinear features.

Morphological operations, including binary thresholding and closing, were applied to create a connectivity map of microglial networks.

**Skeletonization:** A skeletonized representation of microglial structures was generated using iterative thinning. This representation provided insights into microglial ramification patterns associated with vessels.

**Quantification of Ramification Index:** The ramification index, a measure of microglial branching complexity, was calculated for each image using the formula:

$$\text{Ramification Index} = \frac{\text{Total Perimeter} \div \text{Total Area}}{2 \times \sqrt{(\pi \div \text{Total Area})}}$$

Here, perimeter and area represent the total length and coverage of microglial structures, respectively.

**Automated Output Generation:** For each image, the pipeline automatically saved the following:

**Processed Images:** Enhanced microglial connectivity maps and skeletonized networks.

**Quantitative Results:** Ramification indices were compiled into a CSV file for statistical analysis.

### d. Data Processing and Statistical Analysis

Quantitative data were analysed to compare microglial ramification indices across experimental groups (BCAS SHAM, BCAS Vehicle, and BCAS Drug) and vessel types (arteries, veins, micro vessels). Statistical analyses were performed using R (v4.2.0) or GraphPad Prism (v9). Differences between groups were evaluated using one-way ANOVA followed by Tukey's post hoc test. *P* values < 0.05 were considered statistically significant.

### e. Pipeline Availability

The custom MATLAB pipeline used for this analysis, including the main script and supporting functions, is available on GitHub at [https://github.com/aravind245/microglial\\_ramification\\_pipeline](https://github.com/aravind245/microglial_ramification_pipeline). This repository includes sample images, processed results, and detailed instructions for reproducing the analysis.

## 2. eNOS signal intensity analysis

### a. Image Acquisition and Preprocessing

Fluorescence microscopy images of endothelial nitric oxide synthase (eNOS) were acquired as.tif files and stored in a designated directory for batch processing. The raw images were imported into MATLAB using the `imread` function. To minimize noise and enhance contrast, the green fluorescence channel (assumed to contain eNOS signal) was extracted, followed by contrast-limited adaptive histogram equalization

(CLAHE) using `imadjust`. A median filter (`medfilt2`) with a kernel size of 2×2 pixels was applied to reduce speckle noise while preserving structural details. To improve segmentation accuracy, a morphological closing operation (`imclose`) with a 30-pixel disk-shaped structuring element was performed, enhancing continuity in the fluorescence signal.

### b. Segmentation and Feature Extraction

To isolate eNOS-positive regions, the preprocessed images were binarized using adaptive thresholding (`imbinarize`). Small artifacts and background noise were removed using area-based filtering (`bwareaopen`), retaining only objects with an area exceeding 1000 pixels. Border-connected regions were eliminated (`imclearborder`) to prevent artifacts from interfering with intensity calculations. The segmented mask was then applied to the original image, preserving only fluorescence-positive regions for intensity measurement.

### c. Quantification of eNOS Signal Intensity

The largest contiguous eNOS-positive region in each image was identified based on region properties analysis (`regionprops`). The mean fluorescence intensity of this region was computed as a surrogate marker for eNOS expression. If multiple regions were present, only the region with the largest area was selected to ensure signal specificity. The extracted intensity values were stored in a structured results table (`struct2table`) and exported as a.csv file (`writetable`) for downstream statistical analysis.

### d. Data Processing and Output

The script processed all “.tif” images in the input directory, performing batch analysis iteratively. Output results were stored in a dedicated results folder, with each image's extracted intensity value recorded alongside its filename. The complete dataset of intensities was saved as `intensities.csv`, which could be integrated into statistical tools for further analysis.

This automated pipeline enabled quantitative, high-throughput analysis of eNOS fluorescence intensity, reducing manual bias and ensuring reproducibility across multiple image sets. This pipeline is fully available on GitHub at [https://github.com/aravind245/enos\\_signal\\_intensity\\_measurement](https://github.com/aravind245/enos_signal_intensity_measurement).

## Single-cell library preparation from mouse prefrontal cortex tissue

Mice were anesthetized with isoflurane and transcardially perfused with ice-cold, bubbled artificial cerebrospinal fluid (ACSF). The brain was dissected and mounted for sectioning. Coronal brain sections were generated with a vibratome (Leica VT1200). The vibratome chamber was filled with a sucrose-based cutting solution, and sections were cut to a thickness of 250 μm. Sections were subsequently transferred into ice-cold ACSF-Trehalose (ACSFT). Prefrontal cortex regions were excised from individual brain sections. The Paxinos and Franklin's mouse brain atlas was used as reference.

Tissue were digested with Pronase (Sigma-Aldrich, 537088; 2 mg/ml) diluted in bubbled ACSFT at room temperature for 45 min. Subsequently, tissue was washed with 1% FBS in ACSFT three times. Mechanical dissociation of tissue into a single-cell suspension was achieved by pipetting the samples using pipette tips of decreasing bore sizes (p1000, p200, p100, p20). The resultant cell suspensions were filtered through a 0.2 μm cell strainer.

Single-cell suspensions were loaded onto a 10X Genomics Chromium Controller chip by personnel at The Spatial and Single Cell Genomics Platform (S2GP), Genome Institute Singapore (GIS, A\*STAR), targeting the recovery of 6,000 cells. Each animal was prepared as a unique single-cell library using the Chromium Single Cell 3' Reagent Kit (10X Genomics, v. 3.1). Resulting libraries were quantified and evaluated for quality using the High Sensitivity DNA chip on Bioanalyzer Agilent 2100 (Agilent Genomics).

Individual cDNA libraries were pooled equimolarly and sequenced by NovogeneAIT Genomics (Singapore) using the Illumina Nova-Seq6000 platform.

### Analysis of single-cell RNA sequencing data

NovogeneAIT Genomics (Singapore) processed our raw single-cell sequencing data using CellRanger (10X Genomics, v. 6.0.2) and mapped reads to the mouse genome assembly (mm10). The CellRanger software suite converted scRNA-seq data into a count matrix using STAR to align reads to the reference genome, thereby determining the count of unique molecular identifiers (UMIs) mapped to each gene. Count matrices processed via a pipeline built on R/Bioconductor (R v.4.0.2/Bioconductor v.3.12) packages using the *SingleCellExperiment* class (v.1.12.0<sup>71</sup>).

Samples from both sham and BCAS groups were processed under identical experimental conditions, including tissue collection, cell isolation, library preparation, and sequencing. This consistency minimizes technical variability, reducing the need for batch correction. We aimed to capture biologically meaningful differences between sham and BCAS groups within *Pecam1*-expressing endothelial cells, a highly specific and clearly identifiable cell population. In the uncorrected UMAP plots of the *Pecam1*<sup>+</sup> cell population (Supplementary Fig. S2i), cells from both sham and BCAS conditions are intermixed without forming distinct clusters specific to either condition. This indicates minimal technical variability attributable to batch effects. Consequently, we decided to proceed without batch correction to avoid the risk of overcorrecting and potentially obscuring subtle, biologically meaningful differences related to the disease condition.

To assign cluster cell types, we interpreted cluster-enriched genes using *findMarkers* (*scanr* v.1.18.5). We cross-referenced assignments with known prefrontal cortex cell type markers<sup>72</sup>. To elucidate endothelial identities along the arteriovenous zonation, we employed the *AUCell* package (v. 1.12.0<sup>73</sup>) in conjunction with the cluster marker genes established by Vanlandewijck et al.<sup>74</sup>. Raw counts were ranked within each cell, and the Areas Under the ROC Curves (AUC) were calculated for each marker set. The identity attributed to each cell was determined based on the highest AUC value, using the 10% top-ranking genes. We excluded the “AEC2” population due to low cell count, as well as the mixed artery-venous “AVEC” population.

The *edgeR* package (v.3.32.1) was then used to perform pseudobulk differential expression analysis on endothelial subtypes<sup>75</sup>. Differentially expressed genes with *p* adjust-value < 0.05 were considered significant. Metascape was used for biological process enrichment analysis<sup>76</sup>. For membership gene list analysis, the search terms “angiogenesis”, “blood vessel morphogenesis”, “embryonic development”, and “hypoxia”, were applied to GO Biological Processes ontology, using Metascape<sup>76</sup>.

For endothelial-microglial interactions, the CellChat (v.1.6.1)<sup>77</sup> package was employed to infer and analyze intercellular communication networks. For each dataset, the workflow began with extracting the expression matrix and metadata from the *SingleCellExperiment* object, followed by generating a CellChat object using the “createCellChat” function. Ligand-receptor interactions were identified and quantified based on differentially overexpressed ligands and receptors (*p* < 0.05) using the CellChat mouse database and the “identifyOverExpressedInteractions” function. Communication probabilities between cells were inferred by analyzing highly variable genes and pathways through the “computeCommunProb” function. To refine the analysis, we filtered interactions by applying the “filterCommunication” function with a threshold of a minimum of 10 cells per group to ensure robust detection of cell-cell communication signals. Next, we computed pathway-level communication probabilities using the “computeCommunProbPathway” function, which aggregated interaction probabilities across multiple ligands and receptors within each signaling pathway. Visualization of results was carried out using

various functions provided by CellChat. Specifically, “netVisual\_circle” was used to display the number of interactions between cell types, while “netVisual\_chord\_cell” illustrated cell-cell signaling pathways.

### In vivo drug administration of PT2385

Following BCAS surgery, mice were given a 10-day recovery period prior to the initiation of drug or vehicle administration. PT2385 (MCE, HY-12867) was prepared at a concentration of 6 mg/mL using a vehicle of 0.5% methyl cellulose (Sigma-Aldrich, M7027) and 0.5% Tween-80 (Sigma-Aldrich, P5188). Mice were dosed at 30 mg/kg body weight. We have carefully referenced established literature to determine the optimal dosage, administration method, and duration for effective and selective EPAS1 inhibition. PT2385 has been consistently reported in the literature to demonstrate specificity for EPAS1 inhibition at doses ranging from 10 to 60 mg/kg, with durations from a few days up to 12 weeks<sup>27,78–82</sup>. Following the recovery period, BCAS-operated mice were randomly assigned to two groups: one receiving the vehicle *n* = 10 (5 females, 5 males), and another receiving PT2385 *n* = 12 (7 females, 5 males). The sham-operated group received the vehicle only *n* = 13 (6 females, 7 males). All administrations were performed via oral gavage once daily for a total of 30 days. The health and behavior of all animals were closely monitored throughout the study period.

### Behavioral assessments

The open field test was performed in a square white box 40 × 40 × 30 (height) cm for 8 min. The chamber was divided into a central field (center, 20 cm × 20 cm) and an outer field (10 cm border from walls). The mouse's movement was recorded using a video camera, and analyzed using the AnyMaze video tracking system. The center of the animal's body was used as the reference point. The Y-maze comprised three equally spaced arms (120° apart, 35 cm long, and 10 cm wide). The mice were placed in one of the arms (the start arm) and were allowed to explore in the Y-maze for 8 min with access to all three arms. Animals were tracked using AnyMaze software, and the total time and the percent time spent in each arm were analyzed.

### Differentiation of arterial and venous endothelial cells from human pluripotent stem cells

We employed our differentiation protocol of arterial and venous endothelial cells<sup>23</sup>. H9 embryonic stem cells were propagated in mTeSR medium (StemCell Technologies, 85850) on plates coated with Matrigel (Corning, 356234). To seed for endothelial differentiation, H9 were dissociated with accutase (Gibco, A1110501) into single cells, then plated onto Matrigel-coated plates at a density of 50,000 cells/cm<sup>2</sup> in mTeSR1 medium supplemented with 5 μM ROCK inhibitor, Y-27632 (STEMCELL Technologies, 72304). 24 h later, H9 cells were induced towards the mid-primitive streak differentiation pathway with 40 ng/ml recombinant human BMP-4 (R&D Systems, 314-BP/CF), 6 μM CHIR99021 (Sigma-Aldrich, SML1046), 4 μg/ml recombinant human FGF2 (R&D Systems, 233-FB/CF), PIK-90 (Sigma-Aldrich, 528117), recombinant human activin A (R&D Systems, 338-AC/CF) in Chemically Defined Medium (CDM) made up of 50% Ham's F12 (Gibco, 31765092), 50% Iscove's Modified Dulbecco's Medium (IMDM) (Gibco, 31980097), 1 mg/ml polyvinyl alcohol (Sigma-Aldrich, P8136), 1% chemically defined lipid concentrate (Gibco, 11905031), 450 μM 1-thioglycerol (Sigma-Aldrich, M6145), 15 μg/ml transferrin (Roche, 10652202001) and 0.7 μg/ml recombinant human insulin (Roche, 11376497001). After 24 h, mid-primitive streak cells were differentiated into dorsal lateral mesoderm in CDM, supplemented with 40 ng/mL BMP4, 2.5 μM GDC-0941 (STEMCELL Technologies, 73152), 10 μM Forskolin (Tocris, 1099), 2 μM SB505124 (Sigma-Aldrich, S4696), 100 ng/ml VEGF (R&D Systems, 293-VE/CF), 1 μM XAV939 (Tocris, 3748) and 200 μg/mL L-Ascorbic acid 2-phosphate sesquimagnesium salt hydrate (Sigma-Aldrich, A8960)



for 24 h. Following that, the dorsal lateral mesoderm was further differentiated towards either arterial endothelial induction or pre-vein induction, with a duration of 24 h. For arterial induction, CDM supplemented with 15 ng/mL recombinant human activin A, 250 nM DMH-1 (Tocris, 4126), 2.5  $\mu$ M GDC-0941, 100 ng/mL VEGF, 1  $\mu$ M XAV939 and 200  $\mu$ g/mL L-Ascorbic acid 2-phosphate sesquimagnesium salt hydrate was used. For pre-vein induction, CDM comprises 2  $\mu$ M SB505124, 250 nM DMH1, 2  $\mu$ M RO4929097 (MedChemExpress, HY-11102), 100 ng/mL VEGF, 1  $\mu$ M XAV939 and 200  $\mu$ g/mL L-Ascorbic acid 2-phosphate sesquimagnesium. For pre-vein induction, cells were dissociated using accutase and reseeded on Matrigel pre-coated plates at a density of 79,000 cell/cm<sup>2</sup>. Pre-vein cells were differentiated into venous endothelial cells using CDM comprises 2  $\mu$ M SB505124, 2  $\mu$ M RO4929097, 500 nM PD0325901 (Tocris, 4192), 1  $\mu$ M CHIR99021 and 200  $\mu$ g/mL L-Ascorbic acid 2-phosphate sesquimagnesium, with a duration of 24 h. Notably, cells were briefly washed with Dulbecco's Phosphate Buffered Saline (DPBS) (Cytiva, SH30028.03) to eliminate any residual traces of their respective induction medium before proceeding to the next stage of differentiation. Following differentiation, arterial endothelial cells were maintained in EGM-2 media (Lonza, cat no. CC-3162), and venous endothelial cells were maintained in EGM-2 media supplemented with 2  $\mu$ M SB505124 and 2  $\mu$ M RO4929097.

Differentiated arterial and venous endothelial cells were characterized by flow cytometry analysis (Supplementary Fig. S3). Cells were washed with DPBS and dissociated with accutase. Dissociated cells were centrifuged for 5 min at 300  $\times$ g in DPBS, then re-suspended in DPBS and the primary antibodies for arterial and venous endothelial characterization. Cells were stained at 4 °C for 30 min in the dark. Stained cells were washed and resuspended in DPBS, then analyzed with BD LSRFortessa X-20 Cell Analyzer (BD Biosciences), and data acquisition was performed on FACSDiva software (BD Bioscience). Data analysis was performed with FlowJo software v 10.7.1 software (Becton Dickinson). Differentiated arterial and venous endothelial cells with at least 80% and 70% efficiency respectively were used directly for subsequent experiments.

### Experimental settings for in vitro cell culture

Endothelial cells were cultured under 1% oxygen condition using a Hypoxic Incubator Chamber (StemCell Technologies, 27310) placed within a standard incubator. The chamber was purged at a flow rate of 20 L/min for 5 min with a gas mixture of 1% O<sub>2</sub> and 5% CO<sub>2</sub>, balanced with N<sub>2</sub>. For in vitro cell staining for EPAS1, endothelial cell monolayers were fixed with 4% PFA (O9154-85, Nacalai Tesque) at 4 °C, then permeabilized and blocked in 0.1% Triton-X100 and 1% BSA at 4 °C. Primary antibody incubation was done overnight at 4 °C. Secondary antibody staining was done for 1 h at room temperature in the dark. Nuclear counterstaining was performed using DAPI (1:5000). For in vitro PT2385 treatment, endothelial cells were treated with EGM-2 media supplemented with 10  $\mu$ mol/L PT2385 (abcam, ab235501) dissolved in DMSO. Cells were treated with PT2385 during the seeding of cells for tube formation.

### Venous endothelial tube formation

H9-derived venous endothelial cells were thawed and allowed to recover in EGM-2 media (Lonza, cat no. CC-3162) supplemented with 2% heat-inactivated FBS, 1  $\mu$ M ROCK inhibitor, 2  $\mu$ M SB505124, 2  $\mu$ M RO4929097. Venous endothelial cells were then cultured in EGM-2 supplemented with 10% FBS (heat-inactivated) for 24 h prior to dissociating them for tube formation assay. Cells were reseeded onto Geltrex (A1413302, Thermo Fisher Scientific) coated plates at a density of  $6 \times 10^4$  cells/cm<sup>2</sup> in EGM-2 supplemented with 10% FBS and monitored hourly for formation of tube-like structures. Number of tube-like structures was quantified based on the number of well-formed loops per field of view based on reported method<sup>83</sup>.

### Quantitative real-time polymerase chain reaction

Cells were lysed with RLT Buffer, and RNA was extracted using the RNeasy Mini Kit (Qiagen, 74106) according to manufacturer instructions. cDNA synthesis was performed using LunaScript RT SuperMix kit (E3010, New England BioLabs) incubated in a thermal cycler at 25 °C for 2 min, followed by 45 min at 55 °C, and a final step of 1 min at 95 °C. Quantitative PCR (qPCR) was performed with cDNA and the Luna Universal qPCR Master Mix (M3003, New England BioLabs) according to manufacturer instructions. The qPCR reactions were performed using QuantStudio 6 (4485697, Thermo Fisher Scientific). All gene expression data were normalized to the 18S rRNA gene levels. Please refer to Supplementary Table S3 for primer sequences.

### Hi-C visualization

In situ Hi-C sequencing data for human umbilical vein endothelial cells<sup>40</sup>, human aortic endothelial cells (Telo HAEC)<sup>41</sup>, and prefrontal cortex<sup>42</sup> were obtained from the GEO repository (accession numbers: GSE63525, GSE126200, GSE87112, respectively). Visualization of the Hi-C data was performed using the 3D Genome Browser<sup>84</sup> at a resolution of 10 kb covering the region chr2:44760000-47770000.

### Profiling of circulating damaged endothelial cells in human subjects

Human subject PBMCs were stained with antibodies in the dark for 10 min at room temperature, followed by 20 min at 4 °C. Following incubation, cells were washed and resuspended in DPBS with 1% BSA. Flow cytometry was performed using BD LSRFortessa X-20 Analyzer (BD Biosciences), and data acquisition was performed on FACSDiva software (BD Bioscience). Spectral overlap between INDO-1, APC, PE, PE-Cy7, FITC, channels was calculated using a single stain for each channel. Analysis of each subject included at least included 1 million events. Acquired data were analyzed using FlowJo software v 10.7.1 software (Becton Dickinson). CECs were detected by a combined immunophenotypic profile of CD45<sup>+</sup>/CD31<sup>+</sup>/CD133<sup>+</sup>/DNA<sup>+</sup> and were further characterized for the expression of ACKR1. Fluorescence minus one (FMO) controls were used to identify the ACKR1<sup>+</sup> cell population (Supplementary Fig. S8). Antibody details are provided in Supplementary Table S2.

### MRI imaging of cerebrovascular disease burden in human subjects

Patients underwent neuroimaging using MRI. T1- and T2-FLAIR images were used for visual rating of scans based on the modified Fazekas scale for white matter hyperintensity severity<sup>32,33</sup>. The modified Fazekas scale was employed to quantify white matter lesions in four brain regions: right periventricular, left periventricular, right deep subcortical, and left deep subcortical, resulting in a score range of 0–12.

### Human cerebral tissue perfusion by analysis of arterial spin labeling

Two-dimensional pulsed arterial spin labeling (ASL) data were acquired and processed, generating measurements in mL /100 g /min<sup>34</sup>. Briefly, ASL data acquisition utilized FSL's Bayesian Inference for ASL MRI (BASIL) toolbox<sup>35</sup>, and cerebral blood flow was quantified using the Buxton ASL kinetic model<sup>85–87</sup>. Generated cerebral blood flow images were corrected for partial volume effects using BASIL's adaptive spatial prior approach<sup>88</sup>.

### Cognitive assessments in human subjects

The following tests were used for cognitive assessments:

#### Episodic Memory

- Rey Auditory Verbal Learning Test (RAVLT) Delayed
- Anna Tan Delayed (Wechsler Memory Scale (WMS)-IV Logical Memory)
- Rey–Osterrieth Complex Figure (ROCF) Delayed

## Executive Function

- a. Trial Making Test B
- b. Colour Trials 2
- c. Digit Span Backwards

## Processing Speed

- a. Colour Trials 1
- b. WAIS Coding

## Visuospatial

- a. Rey–Osterrieth Complex Figure (ROCF) copy
- b. WAIS Block design (time bonus)

## Language

- a. Naming Test (MoCa Naming + Visual Cognitive Assessment Test (VCAT) Naming)
- b. Semantic fluency animals

Z-scores were derived through the following formula: [(Participant score – mean of cognitively normal)/cognitively normal SD]. The global cognitive score was derived by combining all neuropsychological assessments to get an average score.

## Statistical analysis

The data analysis, excluding the single-cell RNA sequencing data, was performed using GraphPad Prism (v. 10.2.0). Data were tested for normality using the Shapiro-Wilk test. *P* values for data with a single factor were obtained using an unpaired t-test (parametric) or Mann-Whitney test (non-parametric). *P* values for data with multiple comparisons were assessed using a one-way ANOVA (parametric) or Kruskal-Wallis (non-parametric) test. Error bars represent s.d.; \**p* < 0.05, \*\**p* < 0.01, \*\*\**p* < 0.001, \*\*\*\**p* < 0.0001; ns, non-significant.

## Reporting summary

Further information on research design is available in the Nature Portfolio Reporting Summary linked to this article.

## Data availability

The authors declare that all data supporting the findings of this study are available within the paper and Supplementary Information. The raw and processed single-cell RNA sequencing data from this study have been deposited in the NCBI Gene Expression Omnibus database with the accession number: [GSE263191](https://www.ncbi.nlm.nih.gov/geo/query/acc.cgi?acc=GSE263191). Source data are provided with this paper.

## Code availability

The codes for histological image analysis can be accessed from Github repository. The code that was used for analyzing microglial activation was a morphological measure of microglial branching complexity. The microglia ramification index<sup>89</sup> can be found here [[https://github.com/aravind245/microglial\\_ramification\\_pipeline](https://github.com/aravind245/microglial_ramification_pipeline)]. The code that was used for analyzing endothelial vasoactive response was a measurement of eNOS signal intensity<sup>69</sup> and can be found here [[https://github.com/aravind245/enos\\_signal\\_intensity\\_measurement](https://github.com/aravind245/enos_signal_intensity_measurement)].

## References

1. Wiesmann, M., Kiliaan, A. J. & Claassen, J. A. Vascular aspects of cognitive impairment and dementia. *J. Cereb. Blood Flow. Metab.* **33**, 1696–1706 (2013).
2. Brown, W. R., Moody, D. M., Challa, V. R., Thore, C. R. & Anstrom, J. A. Venous collagenosis and arteriolar tortuosity in leukoaraiosis. *J. Neurol. Sci.* **203–204**, 159–163 (2002).
3. Quick, S., Moss, J., Rajani, R. M. & Williams, A. A vessel for change: endothelial dysfunction in cerebral small vessel disease. *Trends Neurosci.* **44**, 289–305 (2021).
4. Vanlandewijck et al. A molecular atlas of cell types and zonation in the brain vasculature. *Nature* **554**, 475–480 (2018).
5. Fischer, A., Zalvide, J., Faurobert, E., Albiges-Rizo, C. & Tournier-Lasserre, E. Cerebral cavernous malformations: from CCM genes to endothelial cell homeostasis. *Trends Mol. Med.* **19**, 302–308 (2013).
6. Lee, H. W. et al. Role of venous endothelial cells in developmental and pathologic angiogenesis. *Circulation* **144**, 1308–1322 (2021).
7. Halder, S. K. & Milner, R. The impact of chronic mild hypoxia on cerebrovascular remodelling; uncoupling of angiogenesis and vascular breakdown. *Fluids Barriers CNS* **18**, 50 (2021).
8. Ishikawa, H. et al. A brief overview of a mouse model of cerebral hypoperfusion by bilateral carotid artery stenosis. *J. Cereb. Blood Flow. Metab.* **43**, 18–36 (2023).
9. Chen, A. et al. Frontal white matter hyperintensities, clasmotodendrosis and gliovascular abnormalities in ageing and post-stroke dementia. *Brain* **139**, 242–258 (2016).
10. Nishio, K. et al. A mouse model characterizing features of vascular dementia with hippocampal atrophy. *Stroke* **41**, 1278–1284 (2010).
11. Shibata, M., Ohtani, R., Ihara, M. & Tomimoto, H. White matter lesions and glial activation in a novel mouse model of chronic cerebral hypoperfusion. *Stroke* **35**, 2598–2603 (2004).
12. Shibata, M. et al. Selective impairment of working memory in a mouse model of chronic cerebral hypoperfusion. *Stroke* **38**, 2826–2832 (2007).
13. Ballabh, P., Braun, A. & Nedergaard, M. Anatomic analysis of blood vessels in germinal matrix, cerebral cortex, and white matter in developing infants. *Pediatr. Res.* **56**, 117–124 (2004).
14. Srinivasan, V. J. et al. Micro-heterogeneity of flow in a mouse model of chronic cerebral hypoperfusion revealed by longitudinal Doppler optical coherence tomography and angiography. *J. Cereb. Blood Flow. Metab.* **35**, 1552–1560 (2015).
15. Wang, J. et al. A new approach for examining the neurovascular structure with phalloidin and calcitonin gene-related peptide in the rat cranial dura mater. *J. Mol. Histol.* **51**, 541–548 (2020).
16. Xiong, B. et al. Precise cerebral vascular atlas in stereotaxic coordinates of whole mouse brain. *Front. Neuroanat.* **11**, 128 (2017).
17. Zhao, L. et al. Pharmacologically reversible zonation-dependent endothelial cell transcriptomic changes with neurodegenerative disease associations in the aged brain. *Nat. Commun.* **11**, 4413 (2020).
18. Barnett, S. N. et al. An organotypic atlas of human vascular cells. *Nat. Med.* **30**, 3468–3481 (2024).
19. Dmitriev, P. M. et al. Vascular changes in the retina and choroid of patients with EPAS1 gain-of-function mutation syndrome. *JAMA Ophthalmol.* **138**, 148–155 (2020).
20. Elvert, G. et al. Cooperative interaction of hypoxia-inducible factor-2alpha (HIF-2alpha) and Ets-1 in the transcriptional activation of vascular endothelial growth factor receptor-2 (Flk-1). *J. Biol. Chem.* **278**, 7520–7530 (2003).
21. Mokhber, N. et al. Cerebral blood flow changes during aging process and in cognitive disorders: a review. *Neuroradiol. J.* **34**, 300–307 (2021).
22. Graff, B. J., Harrison, S. L., Payne, S. J. & El-Bouri, W. K. Regional cerebral blood flow changes in healthy ageing and Alzheimer's disease: a narrative review. *Cerebrovasc. Dis.* **52**, 11–20 (2023).
23. Ang, L. T. et al. Generating human artery and vein cells from pluripotent stem cells highlights the arterial tropism of Nipah and Hendra viruses. *Cell* **185**, 2523–2541.e2530 (2022).
24. Zhang, N. et al. ID1 is a functional marker for intestinal stem and progenitor cells required for normal response to injury. *Stem Cell Rep.* **3**, 716–724 (2014).
25. Schwab, M. et al. Nucleolin promotes angiogenesis and endothelial metabolism along the oncofetal axis in the human brain vasculature. *JCI Insight* **8**, e143071 (2023).

26. Koh, M. Y. & Powis, G. Passing the baton: the HIF switch. *Trends Biochem. Sci.* **37**, 364–372 (2012).
27. Wallace, E. M. et al. A small-molecule antagonist of HIF2 $\alpha$  is efficacious in preclinical models of renal cell carcinoma. *Cancer Res.* **76**, 5491–5500 (2016).
28. Strowd, R. et al. Activity of a first-in-class oral HIF2- $\alpha$  inhibitor, PT2385, in patients with first recurrence of glioblastoma. *J. Neurooncol.* **165**, 101–112 (2023).
29. Dudvarski Stankovic, N., Teodorczyk, M., Ploen, R., Zipp, F. & Schmidt, M. H. H. Microglia-blood vessel interactions: a double-edged sword in brain pathologies. *Acta Neuropathol.* **131**, 347–363 (2016).
30. Chen, S. et al. Microglia and macrophages in the neuro-glia-vascular unit: from identity to functions. *Neurobiol. Dis.* **179**, 106066 (2023).
31. Ng, C. Y. & Cheung, C. Origins and functional differences of blood endothelial cells. *Semin. Cell Dev. Biol.* <https://doi.org/10.1016/j.semcdb.2023.05.001> (2023).
32. Fazekas, F., Chawluk, J. B., Alavi, A., Hurtig, H. I. & Zimmerman, R. A. MR signal abnormalities at 1.5 T in Alzheimer's dementia and normal aging. *Am. J. Roentgenol.* **149**, 351–356 (1987).
33. Vipin, A. et al. Dementia in Southeast Asia: influence of onset-type, education, and cerebrovascular disease. *Alzheimers Res. Ther.* **13**, 195 (2021).
34. Vipin, A. et al. The role of perfusion, grey matter volume and behavioural phenotypes in the data-driven classification of cognitive syndromes. *Alzheimers Res. Ther.* **16**, 40 (2024).
35. Kalucka, J. et al. Single-cell transcriptome atlas of murine endothelial cells. *Cell* **180**, 764–779.e720 (2020).
36. Yang, A. C. et al. A human brain vascular atlas reveals diverse mediators of Alzheimer's risk. *Nature* **603**, 885–892 (2022).
37. Garcia, F. J. et al. Single-cell dissection of the human brain vasculature. *Nature* **603**, 893–899 (2022).
38. Tanner-Eggen, C., Balzer, C., Perrig, W. J. & Gutbrod, K. The neuropsychological assessment of cognitive deficits considering measures of performance variability. *Arch. Clin. Neuropsychol.* **30**, 217–227 (2015).
39. Mahedy, L. et al. Investigation of genetic determinants of cognitive change in later life. *Transl. Psychiatry* **14**, 31 (2024).
40. Rao, S. S. et al. A 3D map of the human genome at kilobase resolution reveals principles of chromatin looping. *Cell* **159**, 1665–1680 (2014).
41. Lalonde, S. et al. Integrative analysis of vascular endothelial cell genomic features identifies AIDA as a coronary artery disease candidate gene. *Genome Biol.* **20**, 133 (2019).
42. Schmitt, A. D. et al. A compendium of chromatin contact maps reveals spatially active regions in the human genome. *Cell Rep.* **17**, 2042–2059 (2016).
43. Halder, S. K. & Milner, R. Mild hypoxia triggers transient blood-brain barrier disruption: a fundamental protective role for microglia. *Acta Neuropathol. Commun.* **8**, 175 (2020).
44. Yata, K. et al. In vivo imaging of the mouse neurovascular unit under chronic cerebral hypoperfusion. *Stroke* **45**, 3698–3703 (2014).
45. Sixt, M. et al. Endothelial cell laminin isoforms, laminins 8 and 10, play decisive roles in T cell recruitment across the blood-brain barrier in experimental autoimmune encephalomyelitis. *J. Cell Biol.* **153**, 933–946 (2001).
46. Lee, H. W., Shin, J. H. & Simons, M. Flow goes forward and cells step backward: endothelial migration. *Exp. Mol. Med.* **54**, 711–719 (2022).
47. Fujita, M. et al. Assembly and patterning of the vascular network of the vertebrate hindbrain. *Development* **138**, 1705–1715 (2011).
48. Bussmann, J., Wolfe, S. A. & Siekmann, A. F. Arterial-venous network formation during brain vascularization involves hemodynamic regulation of chemokine signaling. *Development* **138**, 1717–1726 (2011).
49. Hou, S. et al. Heterogeneity in endothelial cells and widespread venous arterialization during early vascular development in mammals. *Cell Res.* **32**, 333–348 (2022).
50. Xu, C. et al. Arteries are formed by vein-derived endothelial tip cells. *Nat. Commun.* **5**, 5758 (2014).
51. Winkler, E. A. et al. A single-cell atlas of the normal and malformed human brain vasculature. *Science* **375**, eabi7377 (2022).
52. Lau, S. F., Cao, H., Fu, A. K. Y. & Ip, N. Y. Single-nucleus transcriptome analysis reveals dysregulation of angiogenic endothelial cells and neuroprotective glia in Alzheimer's disease. *Proc. Natl. Acad. Sci. USA* **117**, 25800–25809 (2020).
53. Hashimoto, T. & Shibasaki, F. Hypoxia-inducible factor as an angiogenic master switch. *Front. Pediatr.* **3**, 33 (2015).
54. Peng, J., Zhang, L., Drysdale, L. & Fong, G. H. The transcription factor EPAS1/hypoxia-inducible factor 2 $\alpha$  plays an important role in vascular remodeling. *Proc. Natl. Acad. Sci. USA* **97**, 8386–8391 (2000).
55. Lyden, D. et al. Id1 and Id3 are required for neurogenesis, angiogenesis and vascularization of tumour xenografts. *Nature* **401**, 670–677 (1999).
56. Lee, S. B. et al. An ID2-dependent mechanism for VHL inactivation in cancer. *Nature* **529**, 172–177 (2016).
57. Kim, H. J. et al. Inhibitor of DNA binding 1 activates vascular endothelial growth factor through enhancing the stability and activity of hypoxia-inducible factor-1 $\alpha$ . *Mol. Cancer Res.* **5**, 321–329 (2007).
58. Rosenblum, J. S. et al. Developmental vascular malformations in EPAS1 gain-of-function syndrome. *JCI Insight* **6**, e144368 (2021).
59. Lawrence, E. S. et al. Functional EPAS1/HIF2A missense variant is associated with hematocrit in Andean highlanders. *Sci. Adv.* **10**, ead35661 (2024).
60. Gray, O. A. et al. A pleiotropic hypoxia-sensitive EPAS1 enhancer is disrupted by adaptive alleles in Tibetans. *Sci. Adv.* **8**, eade1942 (2022).
61. Csaszar, E. et al. Microglia modulate blood flow, neurovascular coupling, and hypoperfusion via purinergic actions. *J. Exp. Med.* **219**, e20211071 (2022).
62. Masuda, T., Croom, D., Hida, H. & Kirov, S. A. Capillary blood flow around microglial somata determines dynamics of microglial processes in ischemic conditions. *Glia* **59**, 1744–1753 (2011).
63. Haruwaka, K. et al. Dual microglia effects on blood brain barrier permeability induced by systemic inflammation. *Nat. Commun.* **10**, 5816 (2019).
64. Iannucci, J., Rao, H. V. & Grammas, P. High glucose and hypoxia-mediated damage to human brain microvessel endothelial cells induces an altered, pro-inflammatory phenotype in BV-2 microglia in vitro. *Cell Mol. Neurobiol.* **42**, 985–996 (2022).
65. Huntula, S., Saegusa, H., Wang, X., Zong, S. & Tanabe, T. Involvement of N-type Ca(2+) channel in microglial activation and its implications to aging-induced exaggerated cytokine response. *Cell Calcium* **82**, 102059 (2019).
66. Washida, K., Hattori, Y. & Ihara, M. Animal models of chronic cerebral hypoperfusion: from mouse to primate. *Int. J. Mol. Sci.* **20**, 6176 (2019).
67. Gorelick, P. B. et al. Vascular contributions to cognitive impairment and dementia: a statement for healthcare professionals from the American heart association/American stroke association. *Stroke* **42**, 2672–2713 (2011).
68. Sachdev, P. et al. Diagnostic criteria for vascular cognitive disorders: a VASCOG statement. *Alzheimer Dis. Assoc. Disord.* **28**, 206–218 (2014).
69. Leow, Y. J. et al. Biomarkers and Cognition Study, Singapore (BIO-CIS): Protocol, Study Design, and Preliminary Findings. *J. Prev. Alzheimers. Dis.* **11**, 1093–1105 (2024).



70. Harazny, J. M. et al. Increased wall:lumen ratio of retinal arterioles in male patients with a history of a cerebrovascular event. *Hypertension* **50**, 623–629 (2007).
71. Amezquita, R. A. et al. Orchestrating single-cell analysis with Bioconductor. *Nat. Methods* **17**, 137–145 (2020).
72. Bhattacharjee, A. et al. Cell type-specific transcriptional programs in mouse prefrontal cortex during adolescence and addiction. *Nat. Commun.* **10**, 4169 (2019).
73. Aibar, S. et al. SCENIC: single-cell regulatory network inference and clustering. *Nat. Methods* **14**, 1083–1086 (2017).
74. Mae, M. A. et al. Single-cell analysis of blood-brain barrier response to pericyte loss. *Circ. Res.* **128**, e46–e62 (2021).
75. Robinson, M. D., McCarthy, D. J. & Smyth, G. K. edgeR: a bioconductor package for differential expression analysis of digital gene expression data. *Bioinformatics* **26**, 139–140 (2010).
76. Zhou, Y. et al. Metascape provides a biologist-oriented resource for the analysis of systems-level datasets. *Nat. Commun.* **10**, 1523 (2019).
77. Jin, S. et al. Inference and analysis of cell-cell communication using CellChat. *Nat. Commun.* **12**, 1088 (2021).
78. Cheng, X. et al. Marked and rapid effects of pharmacological HIF-2alpha antagonism on hypoxic ventilatory control. *J. Clin. Invest.* **130**, 2237–2251 (2020).
79. Xie, C. et al. Metabolic profiling of the novel hypoxia-inducible factor 2alpha inhibitor PT2385 in vivo and in vitro. *Drug Metab. Dispos.* **46**, 336–345 (2018).
80. Xie, C. et al. Activation of intestinal hypoxia-inducible factor 2alpha during obesity contributes to hepatic steatosis. *Nat. Med.* **23**, 1298–1308 (2017).
81. Xu, J. et al. Increasing AR by HIF-2alpha inhibitor (PT-2385) overcomes the side-effects of sorafenib by suppressing hepatocellular carcinoma invasion via alteration of pSTAT3, pAKT and pERK signals. *Cell Death Dis.* **8**, e3095 (2017).
82. Zhang, J. et al. HIF-1alpha and HIF-2alpha redundantly promote retinal neovascularization in patients with ischemic retinal disease. *J. Clin. Invest.* **131**, e139202 (2021).
83. Bae, E. et al. Integrin alpha3beta1 promotes vessel formation of glioblastoma-associated endothelial cells through calcium-mediated macropinocytosis and lysosomal exocytosis. *Nat. Commun.* **13**, 4268 (2022).
84. Wang, Y. et al. The 3D Genome Browser: a web-based browser for visualizing 3D genome organization and long-range chromatin interactions. *Genome Biol.* **19**, 151 (2018).
85. Chappell, M. A., Groves, A. R., Whitcher, B. & Woolrich, M. W. Variational Bayesian Inference for a Nonlinear Forward Model. *IEEE Trans. Signal Process.* **57**, 223–236 (2009).
86. Alsop, D. C. et al. Recommended implementation of arterial spin-labeled perfusion MRI for clinical applications: a consensus of the ISMRM perfusion study group and the European consortium for ASL in dementia. *Magn. Reson. Med.* **73**, 102–116 (2015).
87. Buxton, R. B. et al. A general kinetic model for quantitative perfusion imaging with arterial spin labeling. *Magn. Reson. Med.* **40**, 383–396 (1998).
88. Chappell, M. A. et al. Partial volume correction of multiple inversion time arterial spin labeling MRI data. *Magn. Reson. Med.* **65**, 1173–1183 (2011).
89. Sivakumar, A. Chronic cerebral hypoperfusion induces venous dysfunction via EPAS1 regulation in mice, Github repository. <https://doi.org/10.5281/zenodo.15493407> (2025).

## Acknowledgements

We thank all participants and clinical coordinators who have contributed to this study through the Dementia Research Centre, Singapore. Special thanks to Ms Karen Chung for animal husbandry, Dr Natalie Yeo for experimental assistance, Dr Aysha Lee-Bansal (Dr Ch'ng Toh Hean's lab)

for antibody, Dr Sharmelee Selvaraji (Prof Lim Kah Leong's lab) for training on BCAS procedures, Dr Anna Barron for scientific discussion, and Mr Tan Kah Junn for help with the BCAS procedure. The work is supported by the Ministry of Education, Singapore, under its Academic Research Funds (MOE2017-T3-1-002, MOE-T2EP30122-0018, and RG88/21), the Strategic Academic Initiative Grant (SP1CLNT900-NTU-A630-PJ-03INP001400A630) and Vascular Research Initiative from the Lee Kong Chian School of Medicine, Nanyang Technological University, Singapore, as well as core funding from Temasek Life Sciences Laboratory. L.T.A. is an Additional Ventures Catalyst to Independence Fellow. C.C. and K.M.L. were Human Frontier Science Program Young Investigators (RGY0069/2019).

## Author contributions

V.K.W. contributed to conceptualization, methodology, formal analysis, investigation, writing of original draft, and visualization. A.M., N.N., H.W., K.Y.T., J.X.S., A.S., S.L., and N.C.T.P. contributed to methodology, formal analysis, and visualization. N.K., A.V., G.S., Y.J.L., and J.X.Y.C. contributed to methodology, resources, and data curation. T.L., M.G., G.D., S.R.L., L.T.A., and K.M.L. contributed to methodology. G.J.A. contributed to resources, supervision, and funding acquisition. C.C. contributed to project administration, conceptualization, formal analysis, investigation, resources, visualization, writing original drafts, supervision, and funding acquisition. All authors were involved in the review and editing of the manuscript.

## Competing interests

The authors declare no competing interests.

## Additional information

**Supplementary information** The online version contains supplementary material available at <https://doi.org/10.1038/s41467-025-61614-3>.

**Correspondence** and requests for materials should be addressed to Christine Cheung.

**Peer review information** *Nature Communications* thanks Xia Yang, Serge Rivest and the other, anonymous, reviewer(s) for their contribution to the peer review of this work. A peer review file is available.

**Reprints and permissions information** is available at <http://www.nature.com/reprints>

**Publisher's note** Springer Nature remains neutral with regard to jurisdictional claims in published maps and institutional affiliations.

**Open Access** This article is licensed under a Creative Commons Attribution-NonCommercial-NoDerivatives 4.0 International License, which permits any non-commercial use, sharing, distribution and reproduction in any medium or format, as long as you give appropriate credit to the original author(s) and the source, provide a link to the Creative Commons licence, and indicate if you modified the licensed material. You do not have permission under this licence to share adapted material derived from this article or parts of it. The images or other third party material in this article are included in the article's Creative Commons licence, unless indicated otherwise in a credit line to the material. If material is not included in the article's Creative Commons licence and your intended use is not permitted by statutory regulation or exceeds the permitted use, you will need to obtain permission directly from the copyright holder. To view a copy of this licence, visit <http://creativecommons.org/licenses/by-nc-nd/4.0/>.

© The Author(s) 2025